Variations of stress field and stone fracture produced at different lateral locations in a shockwave lithotripter field

Gaoming Xiang, Xiaojian Ma, Cosima Liang, et al.

Citation: The Journal of the Acoustical Society of America **150**, 1013 (2021); doi: 10.1121/10.0005823
View online: https://doi.org/10.1121/10.0005823
View Table of Contents: https://asa.scitation.org/toc/jas/150/2
Published by the Acoustical Society of America

ARTICLES YOU MAY BE INTERESTED IN

Model-based localization of deep-diving cetaceans using towed line array acoustic data
The Journal of the Acoustical Society of America **150**, 1120 (2021); https://doi.org/10.1121/10.0005847

A three-dimensional finite difference model for ocean acoustic propagation and benchmarking for topographic effects
The Journal of the Acoustical Society of America **150**, 1140 (2021); https://doi.org/10.1121/10.0005853

A landmark article on nonlinear time-domain modeling in musical acoustics
The Journal of the Acoustical Society of America **150**, R3 (2021); https://doi.org/10.1121/10.0005725

Ultra-sparse metamaterials absorber for broadband low-frequency sound with free ventilation
The Journal of the Acoustical Society of America **150**, 1044 (2021); https://doi.org/10.1121/10.0005850

Experimental realization of an active non-reciprocal metamaterial using an eigen-structure assignment control strategy
The Journal of the Acoustical Society of America **150**, 1092 (2021); https://doi.org/10.1121/10.0005874

Analysis of a passive radio frequency excited acoustic transducer
The Journal of the Acoustical Society of America **150**, 1133 (2021); https://doi.org/10.1121/10.0005848

ASA

Advance your science and career
as a member of the
ACOUSTICAL SOCIETY OF AMERICA

LEARN MORE

JASA ARTICLE

Variations of stress field and stone fracture produced at different lateral locations in a shockwave lithotripter field

Gaoming Xiang,[1,a)] Xiaojian Ma,[1,b)] Cosima Liang,[1] Hongyang Yu,[1] Defei Liao,[1] Georgy Sankin,[1] Shunxiang Cao,[2] Kevin Wang,[2] and Pei Zhong[1,c)]
[1]*Department of Mechanical Engineering and Materials Science, Duke University, Durham, North Carolina 27708, USA*
[2]*Department of Aerospace and Ocean Engineering, Virginia Polytechnic Institute and State University, Blacksburg, Virginia 24061, USA*

ABSTRACT:

During clinical procedures, the lithotripter shock wave (LSW) that is incident on the stone and resultant stress field is often asymmetric due to the respiratory motion of the patient. The variations of the LSW-stone interaction and associated fracture pattern were investigated by photoelastic imaging, phantom experiments, and three-dimensional fluid-solid interaction modeling at different lateral locations in a lithotripter field. In contrast to a *T*-shaped fracture pattern often observed in the posterior region of the disk-shaped stone under symmetric loading, the fracture pattern gradually transitioned to a tilted *L*-shape under asymmetric loading conditions. Moreover, the model simulations revealed the generation of surface acoustic waves (SAWs), i.e., a leaky Rayleigh wave on the anterior boundary and Scholte wave on the posterior boundary of the stone. The propagation of SAWs on the stone boundary is accompanied by a progressive transition of the LSW reflection pattern from regular to von Neumann and to weak von Neumann reflection near the glancing incidence and, concomitantly, the development and growth of a Mach stem, swirling around the stone boundary. The maximum tensile stress and stress integral were produced by SAWs on the stone boundary under asymmetric loading conditions, which drove the initiation and extension of surface cracks into the bulk of the stone that is confirmed by micro–computed tomography analysis.

© *2021 Acoustical Society of America*. https://doi.org/10.1121/10.0005823

(Received 2 March 2021; revised 8 July 2021; accepted 15 July 2021; published online 10 August 2021)

[Editor: Juan Tu] Pages: 1013–1029

I. INTRODUCTION

Despite the rapid advances in ureteroscopy and laser lithotripsy technologies and techniques (Kronenberg and Somani, 2018; Matlaga *et al.*, 2018), shock wave lithotripsy (SWL) has remained the only noninvasive therapy for kidney stone patients in the past three decades (Chaussy *et al.*, 1984; Lingeman *et al.*, 2009; Assimos *et al.*, 2016; New and Somani, 2016; Turk *et al.*, 2016; Alelign and Petros, 2018; Pawar *et al.*, 2018). The clinical treatment efficiency and stone free rate of SWL, however, have been in steady decline because of multiple contributing factors, including (1) a nonidealized pressure waveform with a narrow focal width produced by most contemporary shock wave lithotripters compared to the original HM3 (Qin *et al.*, 2010; Neisius *et al.*, 2014); (2) bubble generation and entrapment in the coupling gel at the interface between the shock wave source and patient (Pishchalnikov *et al.*, 2006); and (3) significant respiratory motion of the patient as a result of increased use of sedation instead of general anesthesia in SWL (Bohris *et al.*, 2003; Pishchalnikov *et al.*, 2006; Leighton *et al.*, 2008; Sorensen *et al.*, 2012). In particular, substantial movement of the target stone during SWL will cause highly variable incident pressure on the stone surface and, consequently, dissimilar fragmentation outcomes (Cleveland *et al.*, 2004; Smith and Zhong, 2013). Although it has been shown previously (Smith and Zhong, 2012; Zhang *et al.*, 2016) that stone comminution in SWL correlates closely with the average positive peak pressure ($p_{+(\mathrm{avg})}$) of the incident lithotripter shock wave (LSW), an in-depth study of the LSW-stone interactions at different locations in a lithotripter field has not been performed. Such knowledge will be important for understanding the dissimilar mechanisms of stone fragmentation and, ultimately, enhancing the clinical treatment success of kidney stone patients using SWL.

Renal calculi are mostly brittle materials that can be disintegrated easily under tension or shear than under compression (Zhong *et al.*, 1993; Freund, 1998). Previous studies (Gracewski *et al.*, 1993; Eisenmenger, 2001; Xi and Zhong, 2001; Cleveland and Sapozhnikov, 2005) have demonstrated various scenarios for the generation of a strong tensile or shear stress inside the stone. In addition, a cohesive zone model of dynamic fatigue (Lokhandwalla and Sturtevant, 2000) has been proposed as a fundamental mechanism for stone fragmentation during SWL. Despite this, most of the prior studies were performed using stone phantoms with simple geometries (e.g., cylinder, sphere, or slab) placed at the lithotripter focus under line symmetric (for simplicity, hereafter referred to as symmetric in this work)

[a)] Electronic mail: gaoming.xiang@duke.edu, ORCID: 0000-0002-3789-1789.

[b)] Current address: Department of Research and Development, China Academy of Launch Vehicle Technology, Beijing, 100076, China. ORCID: 0000-0001-7321-493X.

[c)] Electronic mail: pzhong@duke.edu, ORCID: 0000-0002-2368-6151.

loading conditions. Under such idealized scenarios, the initiation of microcracks and fractures was often observed near the posterior surface of the stone phantom, which were attributed to the phase change (from compression to tension) or wave conversion from longitudinal (or *P*) wave to transverse (or *S*) wave or vice versa with resultant internal wave focusing upon reflection from the stone boundary (Zhong, 2013). For soft stones, such as U-30, strong shear can also be generated by dynamic squeezing at the sharp corners under the special circumstance when a LSW incidents normally to the flat surface of the cylindrical stones (Sapozhnikov *et al.*, 2007). However, for most kidney stones of arbitrary geometry, the creation of a strong shear wave at the stone surface is generally caused by mode conversion of the incident LSW beyond the critical angle for total reflection of the *P* wave inside the stone (Zhong, 2013). Overall, the location of the maximum tensile or shear stress produced in the kidney stones can be influenced by the stone properties, size and geometry, their locations in the lithotripter field, in addition to the characteristics of the incident LSW (Zhang *et al.*, 2016; Neisius and Zhong, 2019). Nevertheless, the correlation between the varying stress field and stone fracture in SWL under clinically prevalent asymmetric loading conditions has not been vigorously investigated.

Numerical simulations can provide valuable physical insight into the evolution of the transient stress field produced by LSW-stone interaction and their potential connections to the resultant fracture patterns produced. Cleveland and Sapozhnikov (2005) constructed a two-dimensional (2D) finite-difference linear elasticity model to analyze the stress field in stones during SWL. The model was later used to calculate the maximum tensile stress produced in cylindrical U30 stones under different exposure conditions with or without the use of acoustic baffles to elucidate the mechanism for dynamic squeezing and correlate with the location of stone fractures observed in the experiments (Sapozhnikov *et al.*, 2007). Other groups have conducted similar investigations by using different stone phantoms and numerical methods (Wijerathne *et al.*, 2010; Wang, 2017). More recently, continuum damage mechanics have been incorporated in the numerical simulations to account for the accumulation of microscopic damage produced by a single or multiple shocks (Fovargue *et al.*, 2018; Cao *et al.*, 2019). Despite these efforts, no previous numerical simulations have been performed to investigate LSW-stone interactions at different locations in a lithotripter field. As such, the stress field and damage potential in the stones under the influence of respiratory motion during SWL are largely unknown.

Furthermore, weak shock reflection at the stone boundary in SWL has not been investigated, although nonlinear wave propagation in fluid, leading to shock and Mach stem formation at the lithotripter focus, has been previously demonstrated (Sturtevant, 1996; Averkiou and Cleveland, 1999; Fovargue *et al.*, 2013). In a few studies that examined the weak shock reflection within the Mach number range (Ms < 1.035) relevant to SWL, the rigid boundary was considered (Marchiano *et al.*, 2007; Karzova *et al.*, 2015). Therefore, the LSW-stone interaction with mode conversion from the pressure wave in the fluid into elastic waves in the solid and surface acoustic waves (SAWs) at the boundary and their possible connection to Mach stem formation and stone fracture have not yet been thoroughly investigated.

In this work, we employ both experimental and computational methods to investigate the variations of stress field and fracture pattern produced at different locations in a shock wave lithotripter field. In the experiments, dynamic photoelastic imaging is used to characterize the generation, propagation, and evolution of various transient stress waves and their interactions inside the PSM-1 (PhotoStress Material) solid phantoms, and stone fracture tests and microCT (μCT) imaging are used to characterize the microcracks in the BegoStone phantoms (BEGO USA, Lincoln, RI). In the numerical computations, a three-dimensional (3D) fluid-solid interaction (FSI) solver, which had been verified and validated for SWL and underwater shock-solid interactions (Farhat *et al.*, 2010; Wang *et al.*, 2011; Wang, 2017; Cao *et al.*, 2019), is used in parallel to quantify the tensile and shear stress fields produced inside the solid phantoms, assess damage potential, and compare with the experimental observations. Moreover, the numerical simulation results are used to facilitate the analysis of SAW generation and propagation, as well as Mach stem formation during LSW-stone interaction, especially under asymmetric loading conditions.

II. MATERIALS AND METHODS

A. Photoelastic imaging

We applied a photoelastic imaging technique to visualize the transient stress field produced by the LSW-stone interaction. The setup was adapted from Xi and Zhong (2001) with minor modifications to incorporate (1) an electromagnetic (EM) shock wave source, (2) a 10 ns pulsed laser for illumination, and (3) a cylindrical stone phantom ($D = 15$ mm and $T = 10$ mm) made of PSM-1 birefringence material (Measurements Groups, Raleigh, NC). Most importantly, photoelastic imaging sequences were captured with the stone phantom placed at various lateral positions in the lithotripter focal plane, and the results were compared with the numerical stimulations.

1. Shock wave source

An axisymmetric EM shock wave generator used in the Siemens Modularis lithotripter was mounted horizontally on the wall of a water tank ($L \times W \times H = 50 \times 30 \times 30$ cm). For cooling purposes, a water reservoir and pump were used to circulate water between the coil and acoustic lens. The acoustic field of the shock wave source has been characterized previously (Neisius *et al.*, 2014). At an output voltage of 14.8 kV, a typical pressure waveform measured at the lithotripter focus is shown in Fig. 1(a), which has a positive peak pressure $p_+ = 52.0$ MPa, a negative peak pressure $p_- = -11.5$ MPa, with a focal width (defined by the full width at half-maximum of p_+) of 7.4 mm and a maximum energy flux density of 0.84 mJ/mm^2. A cylindrical coordinate

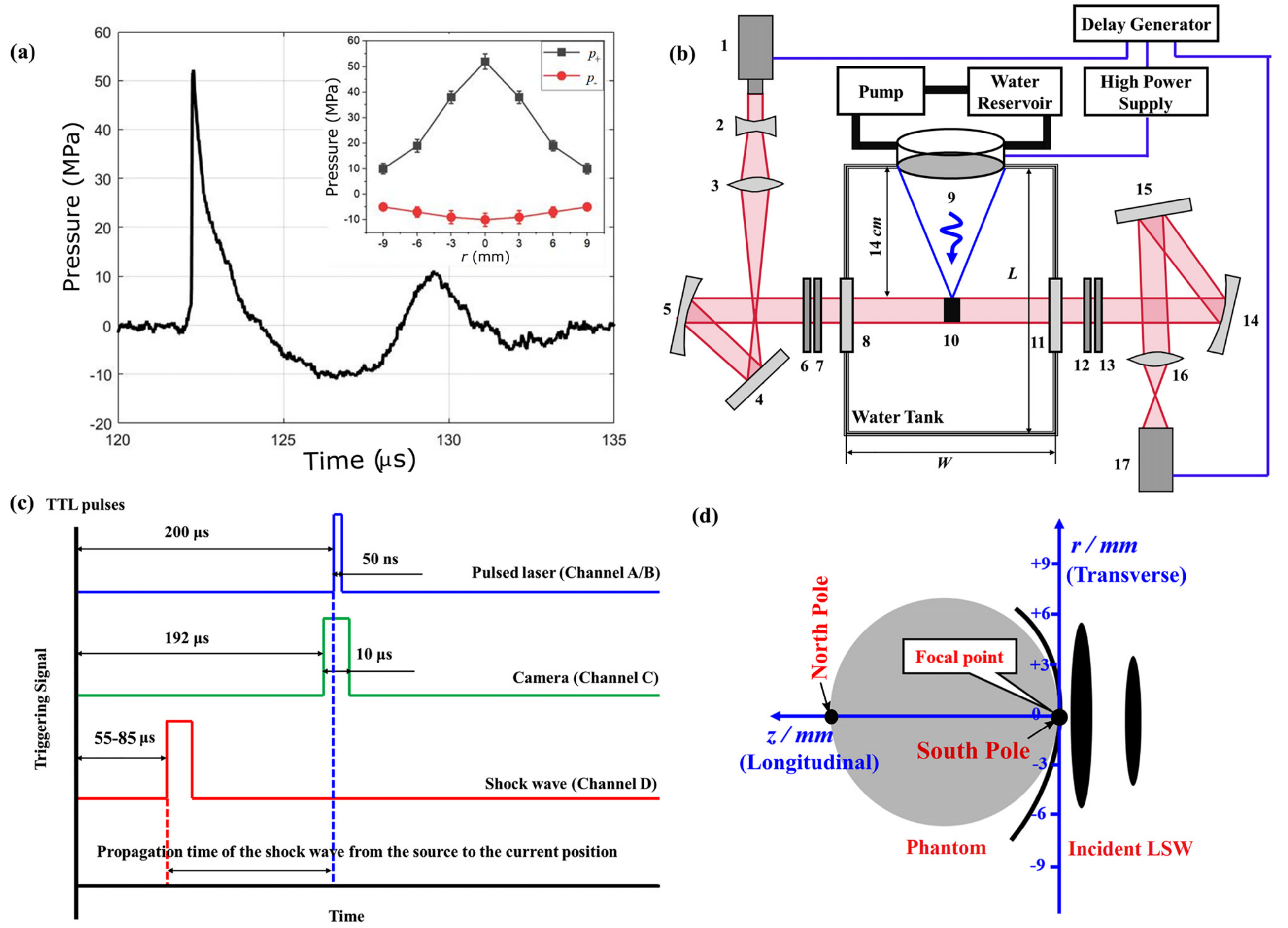

FIG. 1. (Color online) (a) The temporal pressure waveforms measured at the geometric focus of the LSW field and its maximum (p_+) and minimum (p_-) pressure variations in the lithotripter focal plane (i.e., $z = 0$ mm and $r = -9, -6, -3, 0, +3, +6$, and $+9$ mm). (b) The schematic drawing of the experimental setup (top view) (1) laser source, (2) concave lens, (3) convex lens *A*, (4) mirror *A*, (5) spherical schlieren mirror (focus length, 1524 mm) *A*, (6) polarizer, (7) quarter-wavelength plate *A*, (8) water tank glass window *A*, (9) EM shock wave generator, (10) stone phantom, (11) water tank glass window *B*, (12) quarter-wavelength plate *B*, (13) analyzer, (14) spherical schlieren mirror (focus length, 1524 mm) *B*, (15) mirror *B*, (16) convex lens *B*, and (17) high-speed camera. (c) The time sequence diagram illustrating the triggering relationship between the pulsed laser, high-speed camera, and incident LSW. (d) The seven radial positions of the PSM-1 phantom ($D = 15$ mm) that are investigated in this work.

system was set up with its origin ($z = 0$, $r = 0$) aligned with the lithotripter geometric focus, z axis along the LSW propagation direction, and r axis along the transverse radial direction. The inset in Fig. 1(a) shows the radial distribution of p_+ and p_- in the lithotripter focal plane (i.e., $z = 0$ mm).

2. Experimental protocol

Figure 1(b) shows, schematically, the experimental setup for the high-speed shadowgraph and photoelastic imaging (Xi and Zhong, 2001). To visualize the transient stress field in the PSM-1 phantom (Table I) during SWL, a digital delay generator (model 555 pulse/delay generator, BNC, San Rafael, CA) was used to trigger a pulsed laser (SI-LUX-640, Specialised Imaging, Pitstone, UK; wavelength, 640 nm; pulse energy, 2 µJ), a CCD camera (Imager intense, Lavision, Germany), and the shock wave generator. As shown in Fig. 1(c), by adjusting the delay time of the transistor-transistor logic (TTL) trigger pulse with respect to the shock wave generation, a series of high-speed photoelastic and shadowgraph images could be captured at various stages of the incident LSW propagation in water and its interaction with the stone phantom and the resultant stress distribution. As shown in Fig. 1(d), the leading edge of the anterior surface of the PSM-1 phantom was always aligned with the lithotripter focal plane (i.e., $z = 0$ mm), whereas the lateral position of the phantom was varied among $r = +9, +6, +3, 0, -3, -6$, and -9 mm.

B. Stone fracture experiments

Cylindrical stone phantoms (10×5 mm, $D \times T$) were fabricated by thoroughly mixing BegoStone Plus (BEGO USA,

TABLE I. Dimensions and physical properties of the PSM-1 phantom.

Material	Diameter *D* (mm)	Thickness *T* (mm)	Stress optical coefficient *C* (kPa/fringe/m)	Elastic modules *E* (GPa)	Poisson's ratio ν
PSM-1	15.0	10.2	7.0	2.5	0.38

Lincoln, RI) with filtered water at a 5:2 ratio by weight following an established protocol (Esch *et al.*, 2010). Table II summarizes the wave speed data for P (c_P), S (c_S), leaky Rayleigh (c_{LRW}), and Scholte (c_{Scholte}) waves, together with the density (ρ), Young's (E), bulk (K), and shear (G) moduli, as well as Poisson's ratio (ν) of the stone phantom. Before SWL, each phantom was soaked in water for more than 1 h. The anterior surface of the phantom was always aligned with $z = 0$ mm, whereas its lateral position was varied among $r = +9$, $+6$, $+3$, 0, -3, -6, and -9 mm. As shown in Fig. 2(a), the stone phantom was placed in a 3D printed holder with two cylindrical rubber stoppers on the back (diameter, 3.175 mm) and sandwiched between two parallel transparent Mylar films (thickness, 30 μm). In addition, a thin layer of clay (Tack-It, Faber-Castell, USA) was used to adhere the phantom surface on the Mylar film to prevent the phantom from either rotating or translating during SWL. A video camera (HC-V270, Panasonic, Japan) was used to monitor and record the shock wave treatment administered at 14.8 kV and a pulse repetition frequency (PRF) of 0.5 Hz. The number of shocks that were required to initiate the crack and fracture the stone phantom were determined from the video post treatment. In addition, residual stone pieces were collected with the fracture pattern photographed. To ensure consistence, the experiment was repeated six times at each field position. μCT images were acquired at a resolution of 8 μm (Nikon XTH 225, ST, Japan) from additional stone samples either prior to or after 4 and 12 shocks at $r = 0$ mm and -6 mm positions to examine the crack initiation and propagation direction inside the stone.

C. 3D FSI numerical model

In our notation, F and S denote the fluid and solid subdomains occupied by the liquid (i.e., water) and BegoStone, respectively. Given that this is a shock-dominated problem, the fluid is assumed to be compressible and inviscid and, therefore, governed by the following Euler equations expressing the conservation of mass, momentum, and energy:

$$\frac{\partial W(x,t)}{\partial t} = \nabla \mathcal{F}(w) = 0, \quad \forall x \in \Omega_F(t), \quad t > 0, \tag{1}$$

with

$$W = \begin{bmatrix} \rho \\ \rho V \\ \rho e_t \end{bmatrix}, \quad \mathcal{F} = \begin{bmatrix} \rho V^T \\ \rho V \otimes V + p\mathbf{I} \\ (\rho e_t + p) V^T \end{bmatrix},$$

where ρ denotes the fluid density, $V = [u, v, w]^T$ is the fluid velocity vector, and p is the fluid pressure. $e_t = e + \frac{1}{2} V V$ denotes the total energy per unit mass in which e represents the internal energy per unit mass. I is the 3×3 identity matrix.

TABLE II. Physical properties of the BegoStone (5:2 powder-to-water ratio) phantom (Esch *et al.*, 2010).

ρ (kg/m3)	c_S (m/s)	c_P (m/s)	c_{LRW} (m/s)	c_{Scholte} (m/s)	ν	E (GPa)	K (GPa)
1563 ± 23	1813 ± 34	3148 ± 58	1836	1496	0.25	12.9	8.6

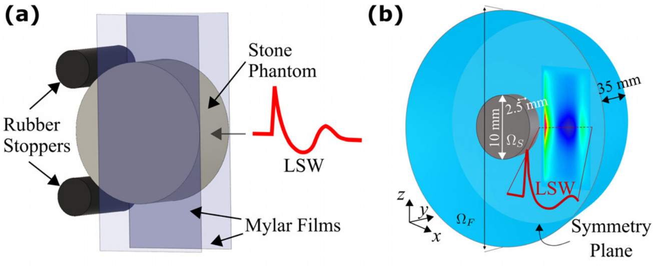

FIG. 2. (Color online) (a) The schematic drawing of the stone holder in the SWL experiment and (b) setup of the numerical simulation. The stone phantom was made of BegoStone with a powder-to-water ratio of 5:2 by weight in a cylinder (diameter = 10 mm and thickness = 5 mm). The LSW was incident from the side surface of the cylinder stone. In the simulation setup, the symmetry plane of the stone phantom was fixed with respect to the lithotripter field, yet the center of the stone could be adjusted along the transverse direction of the incident LSW axis. The plot is not drawn to scale.

Equation (1) is closed by an equation of state (EOS), i.e.,

$$p = (\gamma_L - 1)\rho e - \gamma_L p_L, \tag{2}$$

where $\gamma_L = 6.12$ and $p_L = 343$ MPa for water (Johnsen and Colonius, 2006). The speed of sound in the fluid is calculated based on the EOS as a function of the local density and pressure. The incident LSW is prescribed as the initial condition of the fluid governing equations using the method presented in Cao *et al.* (2019).

Within the solid subdomain, we adopt the Lagrangian frame and solve the following equation of motion that enforces the balance of the linear momentum:

$$\rho_s \ddot{\mathbf{u}}(\mathbf{X}, t) - \nabla \cdot \boldsymbol{\sigma}(\mathbf{u}, \dot{\mathbf{u}}) = \mathbf{b}, \quad \forall \mathbf{X} \in \Omega_S(0), \quad t > 0, \tag{3}$$

where $\mathbf{u}$ denotes the displacement vector in the solid, ρ_s is its density, and $\boldsymbol{\sigma}$ is the Cauchy stress tensor. $\mathbf{b}$ denotes the body force acting in Ω_S, which is assumed to be negligible. We model the BegoStone as a linear elastic and isotropic solid with the constitutive equation given by

$$\boldsymbol{\sigma} = \frac{E\nu}{(1+\nu)(1-2\nu)} tr(\boldsymbol{\epsilon})\mathbf{I} + \frac{E}{1+v}\boldsymbol{\epsilon}, \tag{4}$$

where $\boldsymbol{\epsilon} = \frac{1}{2}\left[\nabla \mathbf{u} + (\nabla \mathbf{u})^T\right]$ is the strain tensor, and E and ν denote the Young's modulus and Poisson's ratio of the material, respectively.

The fluid–solid interface is assumed to be impermeable and governed by two interface conditions, i.e.,

$$(V - \dot{\mathbf{u}}) \cdot \mathbf{n} = 0, \tag{5}$$

$$-p\mathbf{n} = \mathbf{n} \cdot \boldsymbol{\sigma}, \tag{6}$$

which enforce the continuity of normal velocity and traction. $\mathbf{n}$ denotes the outward unit normal to the interface.

We employ a recently developed 3D computational framework, referred to as FIVER (a finite volume method with exact fluid-solid Riemann solvers; Farhat *et al.*, 2010;

Wang *et al.*, 2011; Farhat *et al.*, 2012; Wang *et al.*, 2012; Main *et al.*, 2017), to solve this fluid-solid coupled problem. FIVER couples a finite volume compressible fluid solver with a finite element structural dynamics solver using a second-order accurate partitioned procedure. It enforces the interface conditions using an embedded boundary method, which features the construction and solution of one-dimensional fluid-solid Riemann problems.

Figure 2(b) depicts the setup of the numerical simulations. In the stone fracture experiments described above, the 2D plane that contains the middle cross section of the cylindrical stone can be considered as a symmetry plane. Therefore, only half of the stone in the thickness direction is used in the simulations, and the symmetry boundary condition is enforced in both the fluid and solid solvers. The fluid domain is defined to be a circular cylinder that shares the same axis as the stone with far-field boundaries sufficiently far from the stone so that any wave reflections would not affect the simulation result. The density and linear elastic properties of the stone are specified based on the experimental measurements for soft BegoStone (Table II). The ambient fluid (i.e., liquid water) density and pressure are set to 1000 kg/m^3 and 0.1 MPa, respectively. The incident LSW in the experiments is applied in the simulation as an initial condition for the fluid solver. The radial variation of the incident LSW is approximated by a fourth-order polynomial function, which is fitted to match with the positive peak pressure distribution measured experimentally under the same output setting. The details regarding implementing the initial conditions are described in Cao *et al.* (2019). To simulate stones at various lateral locations with respect to the LSW, we shift the focus of the LSW while the fluid and solid domains are fixed. The solid domain is discretized using a mesh with 574 383 nodes and 3 348 381 tetrahedron elements. The characteristic element size is around 0.052 mm. The fluid domain is discretized using a mesh with 5 414 860 nodes and 34 456 987 tetrahedron elements. In the most refined region (i.e., around the stone), the characteristic element size is 0.05 mm, which is selected based on the grid sensitivity analysis described in Cao *et al.* (2019).

D. Ray tracing analysis and SAW generation at the stone-fluid boundary

To facilitate the interpretation of the numerical simulation results, we have also performed ray tracing analysis of the positions of various stress wavefronts and their evolution inside the stone following previous studies (Gracewski *et al.*, 1993; Xi and Zhong, 2001). As the incident LSW sweeps across the anterior surface of the stone, the incident angle (θ_i) of the LSW will increase from 0° to 90° while traversing through several critical incident angles. Based on the Snell's law, the critical incident angle ($\theta^*_{i(j)}$) for the P or S or leaky Raleigh wave (LRW) in the stone will be reached at

$$\theta^*_{i(j)} = \sin^{-1}\left(\frac{c_L}{c_j}\right), \tag{7}$$

where the subscript j denotes either P or S or LRW with c_j representing their corresponding wave speed either in the solid or at the fluid-solid boundary, respectively, and c_L is the pressure wave speed in the liquid (i.e., water). Usually, the variations of the wave speeds follow the order of: $c_P > c_S > c_{\mathrm{LRW}}\ (>c_L)$. Therefore, based on Eq. (7), the critical incident angle of the stress waves will be reached in the reversed order of $\theta^*_{i(P)} < \theta^*_{i(S)} < \theta^*_{i(\mathrm{LRW})}$. However, previous studies have also shown that c_{LRW} may be larger than c_S but smaller than c_P (Schröder and Scott, 2001).

The leaky Rayleigh wave speed (c_{LRW}) can be obtained by solving the characteristic equation for the SAWs at the solid-liquid boundary (Viktorov, 1967; Zhu *et al.*, 2004; Carcione *et al.*, 2018),

$$4k^2qs - (k^2+s^2)^2 = -i\frac{\rho_L}{\rho}\frac{qk_s^4}{\sqrt{k_L^2-k^2}}, \tag{8}$$

where $q = \sqrt{k^2-k_P^2}$, $s = \sqrt{k^2-k_S^2}$, k, k_P, k_S, and k_L are the wavenumbers of the LRW, P and S waves in the solid, and pressure wave in the liquid, respectively. The real part of the complex roots of Eq. (8) represent c_{LRW} and the real root of Eq. (8) represents the Scholte wave speed (c_{Scholte}), which for soft BegoStone are 1836 m/s and 1496 m/s, respectively. Based on these results and the data in Table II, the critical incident angles ($\theta^*_{i(P)}$, $\theta^*_{i(S)}$, $\theta^*_{i(\mathrm{LRW})}$) for the soft BegoStone are 28.5°, 55.8° and 54.8°, respectively. In addition, the Scholte wave is anticipated to be generated at the glancing incidence of the LSW at the stone boundary.

III. RESULTS

A. Variation of the transient stress field and stone fracture

1. Variation of the transient stress field

Figure 3 shows a compilation of the photoelastic image sequences of the transient stress field produced by the LSW in the cylindrical PSM-1 sample ($D = 15$ mm), placed in the lithotripter focal plane at seven different radial (or lateral) locations. At $r = 0$ mm, all of the stress wavefronts are nearly symmetric both in shape and amplitude with respect to the lithotripter axis, leading to a strong internal wave convergence or focusing. Consequently, the highest fringe order is produced after wave reflection (retarded time, $t' = 14.0\,\mu$s) on the central axis of the sample along the LSW propagation direction at about a distance $D/3$ from the posterior surface. In comparison, at off-axis locations, such as $r = \pm 6$ mm, the stress field becomes asymmetric with higher fringe orders produced on the side of the sample swiped by the incident pressure wavefront. Nevertheless, the focal spot corresponding to the convergence of the reflected waves in the posterior region is still visible at about the same time ($t' = 14.0\,\mu$s), indicating geometric similitude in the LSW-sample interaction at the various radial locations, as revealed by the ray tracing analysis. A detailed and quantitative analysis of the

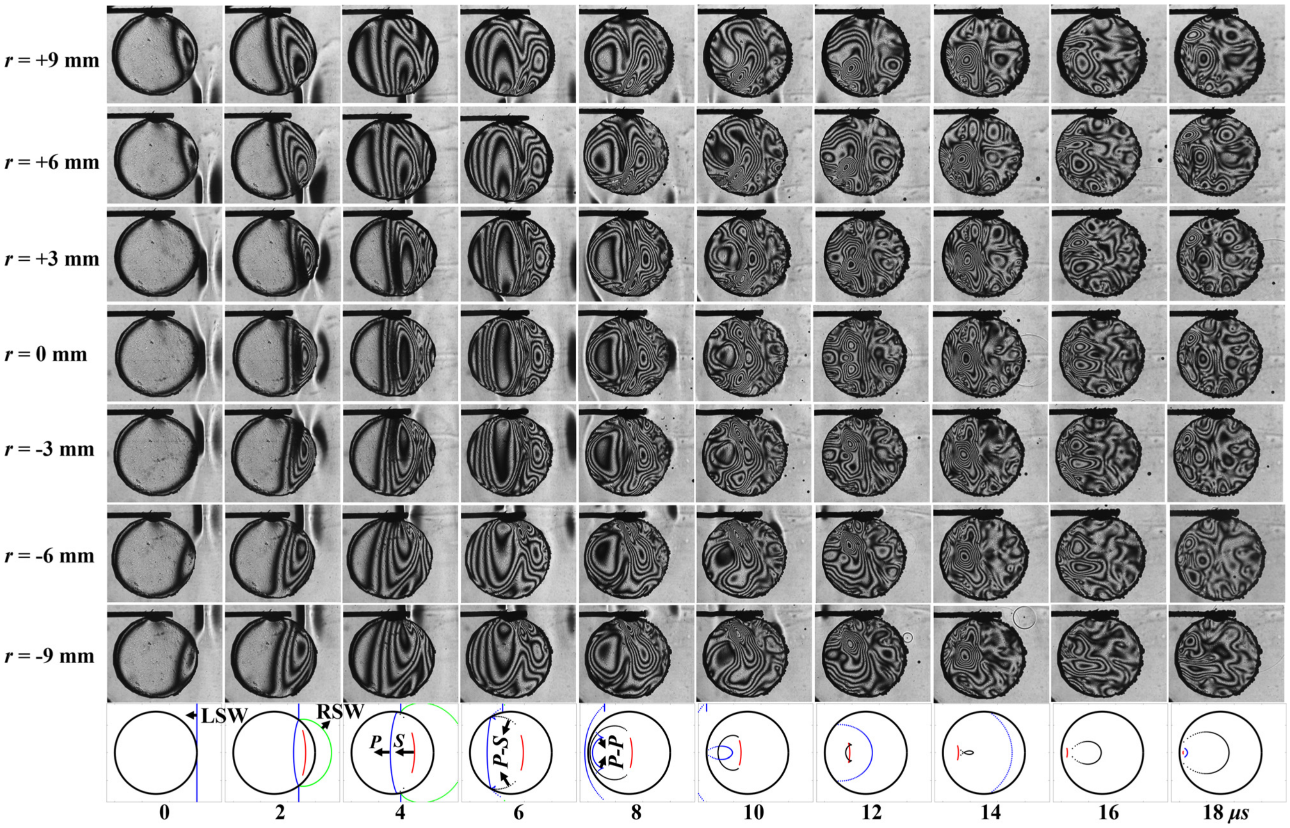

FIG. 3. (Color online) The photoelastic imaging sequence of the LSW interaction with a cylindrical PSM-1 sample ($D = 15$ mm) at different radial positions in the focal plane of the lithotripter, together with the ray tracing analysis of the LSW-PSM-1 sample interaction assuming a plane wave incidence. RSW, reflected shock wave.

LSW-stone interaction, which is based on the numerical simulations, are presented in Sec. III B.

Overall, as the sample is shifted away from the lithotripter axis, the transient stress field will evolve from symmetric to asymmetric with a reduced maximum fringe order inside the stone at increased radial distances. For each pair of samples placed at the same radial distance (i.e., $r = \pm 3$, ± 6, ± 9 mm), their stress fields appear to be a mirror image of each other with respect to the central axis of the lithotripter field (i.e., $r = 0$ mm).

2. Variation in stone fracture

Table III summarizes the number of shocks to create the first visible crack line(s) (N_{vc}) and the number of shocks to fracture the stone (N_f) into two or three separated pieces at different lateral positions. In addition, cavitation erosion with varying crater sizes was observed on the anterior surface of the stone, facing the incident LSW. Representative examples of the crack line formation and fracture pattern, as well as cavitation damage at different lateral positions, are shown in Fig. 4.

TABLE III. Number of pulses to create the first visible crack line(s) and produce stone fracture.

r/mm	−9	−6	−3	0	3	6	9
N_{vc}	26 ± 3	19 ± 5	17 ± 3	17 ± 2	16 ± 4	20 ± 5	31 ± 5
N_f	41 ± 13	34 ± 6	32 ± 6	25 ± 4	30 ± 2	35 ± 4	48 ± 7

As shown in Fig. 4(a), when the incident LSW was aligned with the central axis of the cylindrical stone ($r = 0$ mm), a *T*-shaped crack pattern was consistently observed in the posterior region of the stone while a small crater is produced by the collapse of the cavitation bubbles in or near the focal region of the LSW on the anterior surface of the stone. These two distinctly different damage patterns are separated from each other. The transverse crack was often observed first, initiated from the interior and then propagated outward to the boundary, followed by the longitudinal crack that developed rapidly from the apex of the posterior surface of the stone and intersected with the transverse crack at a distance about $D/3$ from the posterior surface as indicated by the arrows in Fig. 4(b).

When the incident LSW was misaligned with the central axis of the cylindrical stone (e.g., $r = \pm 6$ mm), the two distinct damage patterns would shift to the side of the stone facing the high incident pressure. In addition, the *T*-shaped crack pattern ($r = 0$ mm) was transformed to an *L*-shaped crack pattern ($r = \pm 6$ mm). The number of shocks required to either initiate crack lines or fracture the stone also increased at large off-axis positions ($r = \pm 6$ or 9 mm) in comparison to the on-axis or near-axis positions ($r = 0$ or ± 3 mm). Moreover, the *L*-shaped crack pattern was tilted with respect to the LSW propagation direction, which might

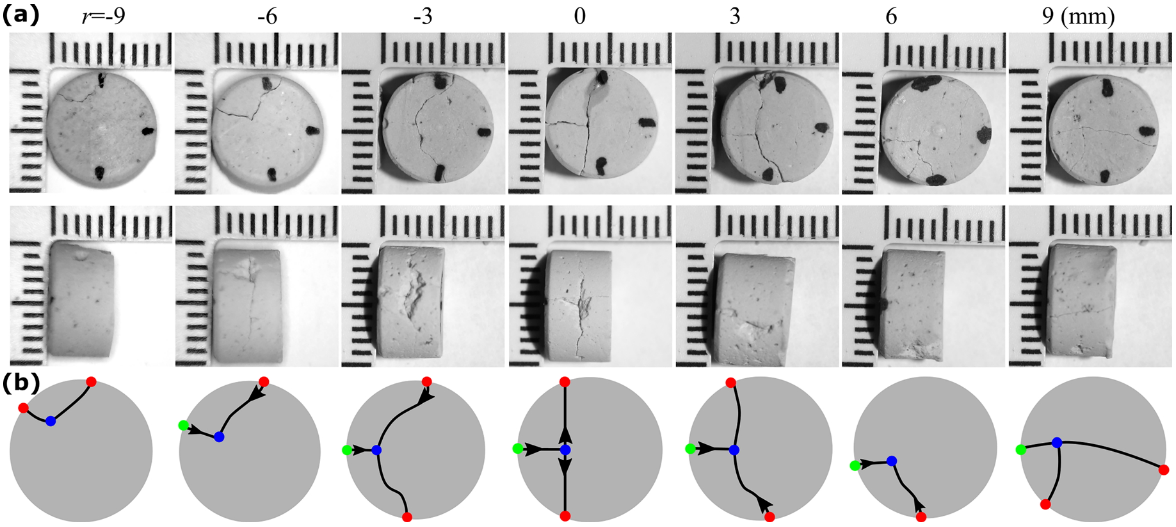

FIG. 4. (Color online) Variations in the fracture pattern of the stone produced at different radial positions in the focal plane of the lithotripter (the incident LSW propagates from right to left in the side view pictures). (a) The side view and front view are shown. (b) The schematic depiction of the crack patterns observed in (a) are shown. The red dots indicate the intersection point of the crack line on the lateral surface of the stone, the green dots indicate the intersection of the crack line with the posterior surface of the stone, and the blue dots indicate the intersection or turning point of the crack lines inside the stone. The arrows indicate the most frequently observed direction of the crack extension.

be caused by the different transient stress field generated inside the stone located at off-axis positions (Fig. 4). The stone fracture patterns produced at $r = \pm 3$ mm appeared to be in transition from symmetric to asymmetric loading conditions. Moreover, the stone fracture patterns produced at $r = \pm 9$ mm varied from the tilted *L*-shaped cracks to rotated *T*-shaped cracks with a horizontal crack line extending to the anterior surface of the stone. The crack lines appeared almost simultaneously on the stone surface, making it difficult to determine their propagation directions.

B. Numerical simulation of LSW-stone interactions at various lateral positions

The dynamic interaction between the incident LSW and target stone generates different stress waves and their transient interactions inside the stone, together with multiple reflected, head or leaky pressure waves in the surrounding fluid. To dissect this complex process responsible for producing the evolving stress field and resultant stone fracture pattern, we will first compare the numerical simulation results of the stress field produced under symmetric vs asymmetric loading conditions. Next, we will analyze the evolution of the maximum tensile stress, stress integral (SI), and the corresponding pressure near the stone boundary in relation to different mode conversions and weak shock reflection at a fluid-solid boundary with the formation of a Mach stem.

1. Under the symmetric loading condition ($r = 0$ mm)

Figure 5 depicts the general features in the LSW-stone interaction and resultant evolution of the newly generated wavefronts in both the stone and surrounding fluid under idealized symmetric loading conditions, which promote wave focusing inside the stone. Snapshots of the distribution in the divergence or div($\nabla \cdot \mathbf{u}$) and curl ($\nabla \times \mathbf{u}$) of the displacement field ($\mathbf{u}$), maximum tensile stress ($\sigma_{\max}$), and maximum shear stress ($\tau_{\max}$) inside the stone, as well as the pressure field in the surrounding fluid are presented, together with the ray tracing plots of various wavefronts. The retarded time $t' = 0$ is set for the moment when the incident LSW first contacts the anterior surface at the south pole of the stone [see Fig. 1(b)]. Several critical moments in this transient interaction are described as follows.

(1) In the early stage of the interaction when $\theta_i < \theta^*_{i(P)}$ (e.g., $t' = 0.99\,\mu$s), both *P* and *S* waves are generated instantaneously on the stone boundary at the contact point of the incident LSW with the *P* wavefront advancing forward faster and also at a larger refraction angle than the *S* wavefront inside the stone as shown by div and curl, respectively. The *P* wavefront is in a convex shape with high compressive stress produced in its central portion, followed by the *S* wavefront, which is relatively flat yet with high shear stress produced at its peripheral near the contact point on the boundary. Simultaneously, a reflected shock wave (RSW) is generated in the fluid, moving backward away from the anterior surface of the stone, leading to a high-pressure region covering the irradiated stone boundary.
(2) Next, when $\theta^*_{i(P)} < \theta_i < \theta^*_{i(S)}$ (e.g., $t' = 1.30\,\mu$s), the advancing *P* wavefront has detached from the contact point while the *S* wavefront in the stone and the RSW in the fluid are still in contact with the incident LSW on the boundary. As a result, while the central portion of the *P* wavefront is advancing freely, its peripheral ends will be reflected and refracted from the lateral surface of the stone, generating both the reflected *P* wave (i.e., *P*-*P*) and reflected *S* wave (i.e., *P*-*S*) back into the stone, and a refracted head pressure wave (H_P) into the fluid

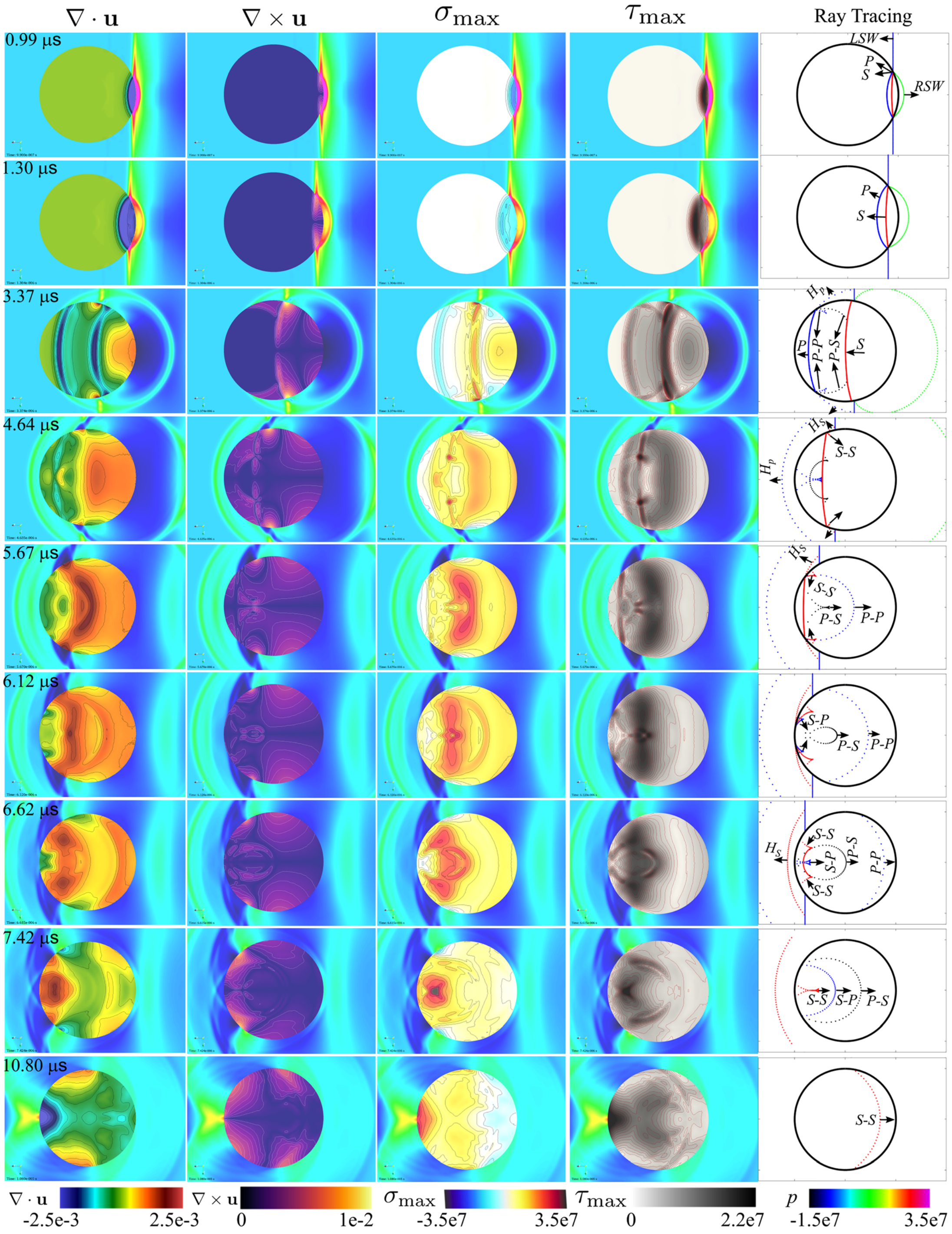

FIG. 5. (Color online) The numerical simulations of the LSW-stone interaction under the symmetric loading condition. The incident LSW is a planar wavefront, line symmetric with respect to the central axis of a soft cylindrical BegoStone phantom ($D = 10$ mm, $H = 5$ mm) with its front surface center aligned with $z = 0$ mm and $r = 0$ mm (see Fig. 1). The divergences ($\nabla \cdot \mathbf{u}$) and curls ($\nabla \times \mathbf{u}$) of the displacement field, maximum tensile stress ($\sigma_{\max}$), and maximum shear stress ($\tau_{\max}$) inside the stone are shown together with the ray tracing analysis of various wavefronts both in the stone and surrounding fluid. *P* and *S*, refracted *P* wave and *S* wave generated at the anterior surface of the stone; *P-P* and *P-S*, *P* and *S* waves inside the stone generated by the reflection of the refracted *P* wave from the lateral and posterior surfaces of the stone; H_P, head pressure wave generated by the refraction of the advancing *P* wave along the stone boundary; H_S, head pressure wave generated by the refraction of the advancing *S* wave along the stone boundary; *S-P* and *S-S*, *P* and *S* waves inside the stone generated by the reflection of the refracted *S* wave from the lateral and posterior surfaces of the stone. The unit for the stress or pressure is Pa.

following Snell's law. In contrast, the *S* wave is generated at the contact point and continuously strengthened on the boundary by the incident LSW through mode conversion. Moreover, the RSW in the fluid begins to encounter the tensile component of the incident LSW, leading to reduced pressure near the anterior surface of the stone. At this moment, the effects of the reflected *P-P* and *P-S* waves on the overall stress field and refracted H_P wave on the surrounding pressure field are not pronounced.

(3) When $\theta^*_{i(S)} < \theta_i < 90°$ (e.g., $t' = 3.37\,\mu$s), the *P-P* and *P-S* wavefronts grow near the stone boundary, and the H_P generated by the detached *P* wavefront, advancing along the stone boundary, is visibly pronounced. Because the *P* wave is reflected inside the stone from a pressure-release boundary, the tensile and shear stresses are built up by the *P-P* and *P-S* wavefronts in front of the advancing *S* wavefront. However, the fluid region covered by the H_P wavefront in front of the incident LSW is still under weak compression. Moreover, the *S* wavefront inside the stone has also detached from the contact point, advancing to produce a reflected *S* wave (i.e., *S-S*) from the lateral surface of the stone and a refracted head pressure wave (H_S) into the fluid. During this period, the LRW is anticipated to be generated, which will be discussed in Sec. III B 2 when such a SAW mode conversion becomes stronger under asymmetric loading conditions.

(4) Furthermore, at $t' = 4.64\,\mu$s, when the incident LSW has passed the equator of the stone or $\theta_i > 90°$, the advancing *P* wavefront has reached the north pole [i.e., the furthest point in the stone from the incident LSW as indicated in Fig. 1(d)], and the reflected and converging *P-P* wavefronts (from the top and bottom halves) meet and cross on the central axis, producing the first high tensile spot near the posterior surface of the stone. In comparison, the *S-S* wavefront is growing near the boundary. Two additional high tensile stress spots are produced off the central axis of the stone by the interaction of the reflected *P-S* wavefront with the advancing *S* wavefront. Moreover, the refraction of the advancing *S* wavefront at its peripherals on the lateral stone boundary generates the H_S wave, which radiates the pressure wave into the fluid in front of the LSW. Simultaneously, the reflected *S-S* wavefront produced inside the stone grows substantially near the lateral surface, generating tension in a small region underneath the boundary covered by the H_S wavefront.

(5) Subsequently, at $t' = 5.67\,\mu$s, the converging *P-S* wavefronts meet and cross the central axis, producing focal spots of high shear stresses. Moreover, high shear and tensile stresses are produced in a broad central region posterior to the stone equator by the interaction of the advancing *S* wavefront with the reflected *P-P* wavefront moving in opposite directions. In comparison, the shear stresses produced by the reflected *S-S* wavefronts near the lateral boundary of the stone are relatively weak, although the region covered by the H_S wavefront in the fluid ahead of the incident LSW continues to increase.

(6) At $t' = 6.12\,\mu$s, when the advancing *S* wavefront on the posterior surface of the stone reaches a position with $\theta_i < \theta^*_{i(P)}$ from the solid side, a reflected *P* wave (i.e., *S-P*) will be generated on the boundary together with the *S-S* wavefront. The posterior region under high tensile and shear stresses continues to advance toward the north pole while extending laterally. This high stress region coincides with the area where the transverse crack formation is observed in the stone fracture experiments (Fig. 4, $r = 0$ mm). In addition, a focal region of high tensile and shear stresses produced by the convergence of the *P-S* wavefronts crossing the central axis of the stone is clearly visible.

(7) At $t' = 6.62\,\mu$s, the posterior region of the stone is covered by the reflected *S-P* and *P-S* waves, both moving toward the anterior surface of the stone. Furthermore, two side lobes of high tensile and shear stresses are produced by the reflected *S-S* waves from the lateral surfaces.

(8) At $t' = 7.42\,\mu$s, the reflected *S-S* wavefront converges across the central axis of the stone, producing the maximum tensile stress inside the stone. Similarly, the convergence of the earlier reflected *P-P*, *P-S*, and *S-P* wavefronts creates a moving focal spot of high tensile and shear stresses along the central axis of the stone, which coincides with the formation of the longitudinal crack observed in the stone fracture experiments (Fig. 4, $r = 0$ mm).

(9) At $t' = 10.80\,\mu$s, high tensile and shear stresses are observed at the north pole of the stone far behind the reflected *S-S* wavefront as a result of the convergence of the SAWs along the stone boundary as shown in Sec. III B 2.

2. Under the asymmetric loading condition ($r = -6$ mm)

Figure 6 shows a representative example of the asymmetric LSW-stone interaction ($r = -6$ mm). Whereas the geometric features of the interaction remain the same, the peak pressure of the incident LSW is shifted off the central axis of the stone, leading to asymmetric stress distribution inside the stone with less internal wave focusing. Therefore, only the upper half of the stone subjected to higher incident pressure of the LSW will be discussed, as shown in the ray tracing analysis, unless otherwise noted. Here, we will focus on the prominent features observed on the stone-fluid boundary in relation to the mode conversion, SAW generation and propagation, as well as the Mach stem formation.

(1) When $\theta_i < \theta^*_{i(P)}$ (e.g., $t' = 0.99\,\mu$s), the incident pressure increases progressively with θ_i in the upper half, leading to significantly stronger compressive and shear stresses generated inside the stone and, simultaneously, stronger reflected pressure in the surrounding fluid compared to the corresponding values in the lower half of the stone where the incident pressure decreases with θ_i.

(2) When $\theta^*_{i(P)} < \theta_i < \theta^*_{i(S)}$ (e.g., $t' = 1.30\,\mu$s), strong shear is generated at the contact point on the stone boundary after the detachment of the *P* wavefront. Concomitantly, the RSW in the fluid is intensified.

(3) When $\theta^*_{i(S)} < \theta_i < 90°$ (e.g., $t' = 3.37\,\mu$s), the incident LSW in the fluid has just detached from the stone surface. Correspondingly, the *S* wavefront starts to detach from the contact point, and the stress field in the solid is dominated by two distinct humps, which are clearly visible in the div with one in the tension (denoted by "*"), produced by the reflected *P-P* and *P-S* wavefronts in

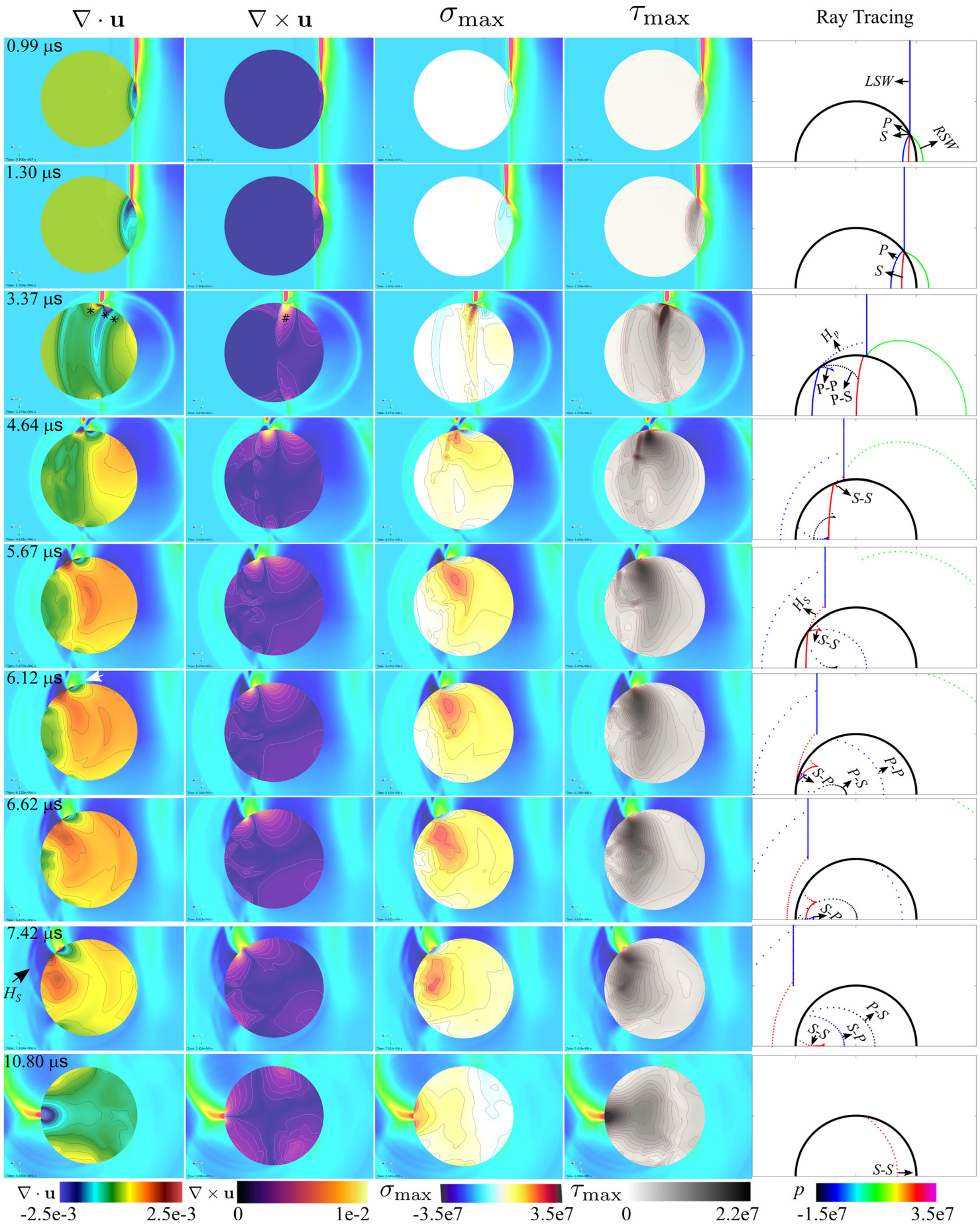

FIG. 6. (Color online) The numerical simulations of the LSW-stone interaction under the asymmetric loading condition. The incident LSW is a planar wavefront with its central axis aligned off-axis at $z = 0$ mm and $r = -6$ mm (see Fig. 1) with respect to a soft cylindrical BegoStone phantom ($D = 10$ mm, $H = 5$ mm). The divergences ($\nabla \cdot \mathbf{u}$) and curls ($\nabla \times \mathbf{u}$) of the displacement field, maximum tensile stress ($\sigma_{\max}$), and maximum shear stress ($\tau_{\max}$) inside the stone are shown together with a ray tracing analysis of various wavefronts both in the stone and surrounding fluid. *P* and *S*, refracted *P* wave and *S* wave generated at the anterior surface of the stone; *P-P* and *P-S*, *P* and *S* waves inside the stone generated by the reflection of the refracted *P* wave from the lateral and posterior surfaces of the stone; H_P, the head pressure wave generated by the refraction of the advancing *P* wave along the stone boundary; H_S, the head pressure wave generated by the refraction of the advancing *S* wave along the stone boundary; *S-P* and *S-S*, *P* and *S* waves inside the stone generated by the reflection of the refracted *S* wave from the lateral and posterior surfaces of the stone. The unit for the stress or pressure is Pa.

association with the H_P wavefront in front of the incident LSW, followed by the other in compression (denoted by "**") created by the RSW. Moreover, these two humps are jointed at the saddle point by an elongated protrusion in the curl and associated strong shear (and tensile) stress (denoted by "#"), riding in between the two humps. Together, they form a triple-feature structure (i.e., hump-saddle-hump). The simultaneous appearance of div and curl on the boundary is a strong indication for the generation and propagation of SAWs (Cleveland and Sapozhnikov, 2005; Zhang *et al.*, 2019)), such as the LRW characterized by the convergence of a leading transverse branch (represented by the saddle) and a trailing longitudinal branch (represented by the second hump) as shown in Zhang *et al.* (2019).

(4) When $\theta_i > 90°$ (e.g., $t' = 4.64\,\mu$s), the triple-feature structure on the stone boundary further intensifies as the incident LSW sweeps across the equator of the stone. On the fluid side, the H_S generated tensile pressure grows significantly in front of the LSW and, together with the compressive pressure footprint behind the RSW, form the counterparts of the two humps on the solid side. At this moment, the incident LSW front has clearly detached from the stone boundary, cut through by the wavefronts of the H_S and, presumably, the Schmidt head wave associated with the LRW (Zhang *et al.*, 2019). In addition, the region covered by the protrusion rider in the curl expands laterally, creating a region with diffused high shear and tensile stresses. In contrast, the high tensile and shear stress regions typically observed along the central axis of the stone under the symmetric condition (i.e., $r = 0$ mm) have disappeared because of the asymmetric pressure distribution around the stone.

(5) At $t' = 5.67\,\mu$s, the H_S generated tensile pressure region grows further while the ensuing RSW-generated hump does not change significantly. The curl region continues to expand with diffused high shear and tensile stresses in the posterior region of the stone.

(6) At $t' = 6.12\,\mu$s, the triple-feature structure continues to grow while moving progressively along the boundary toward the north pole of the stone. Behind the fin-shaped region covered by the H_S and intersected by the detached LSW, a Mach stem aligned along the surface normal direction of the stone has emerged, which could be initiated by the incident LSW glancing through the equator of the stone.

(7) Toward the end of the interaction from $t' = 6.62\,\mu$s to $t' = 7.42\,\mu$s, the Mach stem in the fluid continues to grow in strength and length while the enlarged region with diffused high shear and tensile stresses inside the stone moves closer to the north pole. Evidence of the convergence of the wavefronts (by *S*-*P* and *S*-*S*) is noticeable, albeit much weaker than for $r = 0$ mm. Moreover, the posterior surface of the stone is completely covered by the asymmetric envelop of the H_S wavefronts from both the upper and lower halves of the stone.

(8) At $t' = 10.8\,\mu$s, the Mach stem behind the fin-shaped region covered by the H_S reaches the north pole, generating a combination of shear and tensile stresses near the boundary.

3. Variations of the stress field inside and along the stone boundary

To recapitulate different stress wavefronts and SAWs, we have extracted data from virtual sensors imbedded both inside the stone and near the fluid-solid boundary from samples placed at four lateral positions ($r = 0$, -3, -6 and -9 mm). Using these data, we quantify the evolution of the first principal stress (i.e., $\sigma_{\max}$) in the solid and pressure in the fluid during the LSW-stone interaction. Hereafter, as shown in Fig. 7(a), all of the sensors were located along different rays or near the stone boundary in the symmetric plane of the computational domain.

Figures 7(b) and 7(c) depict the variation of $\sigma_{\max}$ along two rays normal to the refracted *S* wavefront in the sample placed at $r = 0$ mm when θ_i increases from 0° (ray 1, which coincides with the ray at the *P* wavefront) to 25° (ray 2). The sensor data first reveal a compressive (negative) peak associated with the *P* wave (3086 m/s), followed by the tensile (positive) peak generated by the *S* wave (1852 m/s), which is consistent with the features of the stress field observed in Fig. 5. More importantly, waveforms of $\sigma_{\max}$ near the solid boundary (i.e., ray 3 along $r_S = 4.95$ mm) reveal LRW propagation in the range of $60° < \theta_i < 90°$ [Fig. 7(d)] and Scholte wave propagation in the range of $110° < \theta_i < 180°$ [Fig. 7(e)]. The LRW propagation is accompanied by the generation of strong tensile stress at the stone boundary, augmented beyond $\theta^*_{i(S)}$ by the refracted *S* and associated *S*-*S* waves propagating near the stone boundary [Figs. 6 and 7(f)]. Because the simultaneous propagation of an evanescent wave (EW) in the fluid during this period near the stone boundary (Eisenmenger 2001), the peak in $\sigma_{\max}$ is only reached when the LRW is sufficiently separated from the EW (Zhang *et al.*, 2019). In addition, the progressive convergence of the peak in $\sigma_{\max}$ along the same radial direction from $r_S = 4$ mm to $r_S = 4.95$ mm beyond $\theta^*_{i(S)}$ (or 60 °), as shown in Fig. 7(f), supports the notation that the maximum tensile stress is indeed generated by the LRW. This conclusion is also consistent with the fact that the peak in $\sigma_{\max}$ on the stone boundary is always produced at $\theta_i = 75°$, independent of the radial positions of the stone in the lithotripter field [Fig. 7(g)]. It is worth noting that higher peak $\sigma_{\max}$ values are obtained at $r = -3$ mm (61.0 MPa) and $r = -6$ mm (53.6 MPa) than at $r = 0$ mm (38.8 MPa), indicating that the experimentally observed "*L*-shaped" cracks in Fig. 4(b) may initiate from the stone boundary under those asymmetric loading conditions.

4. Variations of the pressure and weak shock reflection along the stone boundary

Although weak shock wave reflection from a rigid boundary has been studied extensively (Zakharian *et al.*, 2000; Skews and Ashworth, 2005; Baskar *et al.*, 2007), such an analysis has not been performed for the LSW-stone interaction. In particular, the transition from regular reflection (RR) with two-shock structure (i.e., incident and reflected shocks) to irregular reflection (IR) with three-shock structure, characterized by the detachment of the point of intersection T of the incident and reflected shocks from the boundary and the formation of a new shock front (i.e., Mach stem) that connects T to the stone surface, has not been reported in SWL. Because our numerical model incorporates fluid compressibility and can be used to characterize the

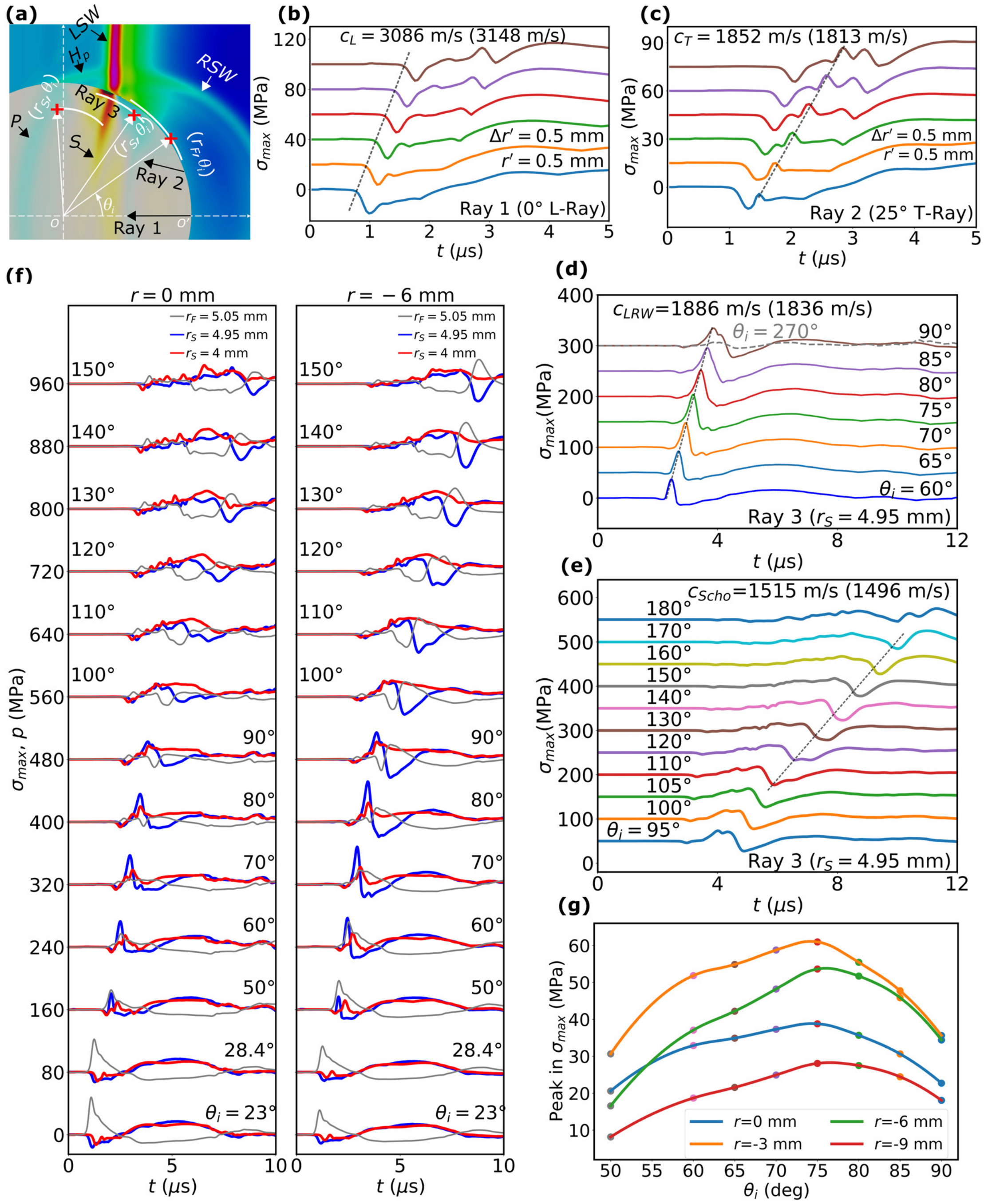

FIG. 7. (Color online) The variations of the stress and pressure monitored by sensors placed inside the stone and along the stone-fluid boundary. (a) A schematic diagram illustrating various stress wavefronts in the solid and pressure wavefronts in the fluid at a retarded time of 2.1 μs. Ray 1 overlaps with the P wavefront at 0° refraction angle, ray 2 corresponds to the S wavefront at 25° refraction angle, and ray 3 is along the circumferential direction of the stone boundary at a radius $r_S = 4.95$ mm. The corresponding sensors located on the fluid side have a radius $r_F = 5.05$ mm. [(b),(c),(d),(e)] The time history of the maximum principal stress $\sigma_{\max}$ along ray 1, ray 2, and ray 3. (f) The time history of $\sigma_{\max}$ at $r_S = 4.00$ and 4.95 mm and pressure at $r_F = 5.05$ mm along different radial directions from the center of the stone, responding to different θ_i. The stone was placed either at $r = 0$ mm or $r = -6$ mm in the lithotripter field. (g) The variations in the peak value of $\sigma_{\max}$ with θ_i produced in stones treated at four different off-axis locations in the lithotripter field. Note that the vertical scale of adjacent curves in (b), (c), (d), and (e) are offset by 20, 15, 50, and 50 MPa, respectively. The vertical scale of the adjacent curves in (f) are offset by 80 MPa. The results of (b) and (c) are produced under the condition of $r = 0$ mm, and the results of (d) and (e) are produced under the condition of $r = -6$ mm.

nonlinear propagation of the LSW, we further analyze the pressure data from sensors located along various surface normal directions ($\theta_i = 23$ °–180 °). Moreover, as shown in Fig. 8(a), for each normal direction, sensor data are extracted at four different radial distances ($r_F = 5.05$, 5.25, 5.50, and 5.75 mm) from the stone center to dissect the evolution of various pressure and weak shock waves in the fluid near the stone boundary.

The reflection of a weak shock wave ($Ms < 1.05$) from a rigid boundary has been shown to depend on a critical parameter a, which is given by (Baskar *et al.*, 2007; Karzova *et al.*, 2015)

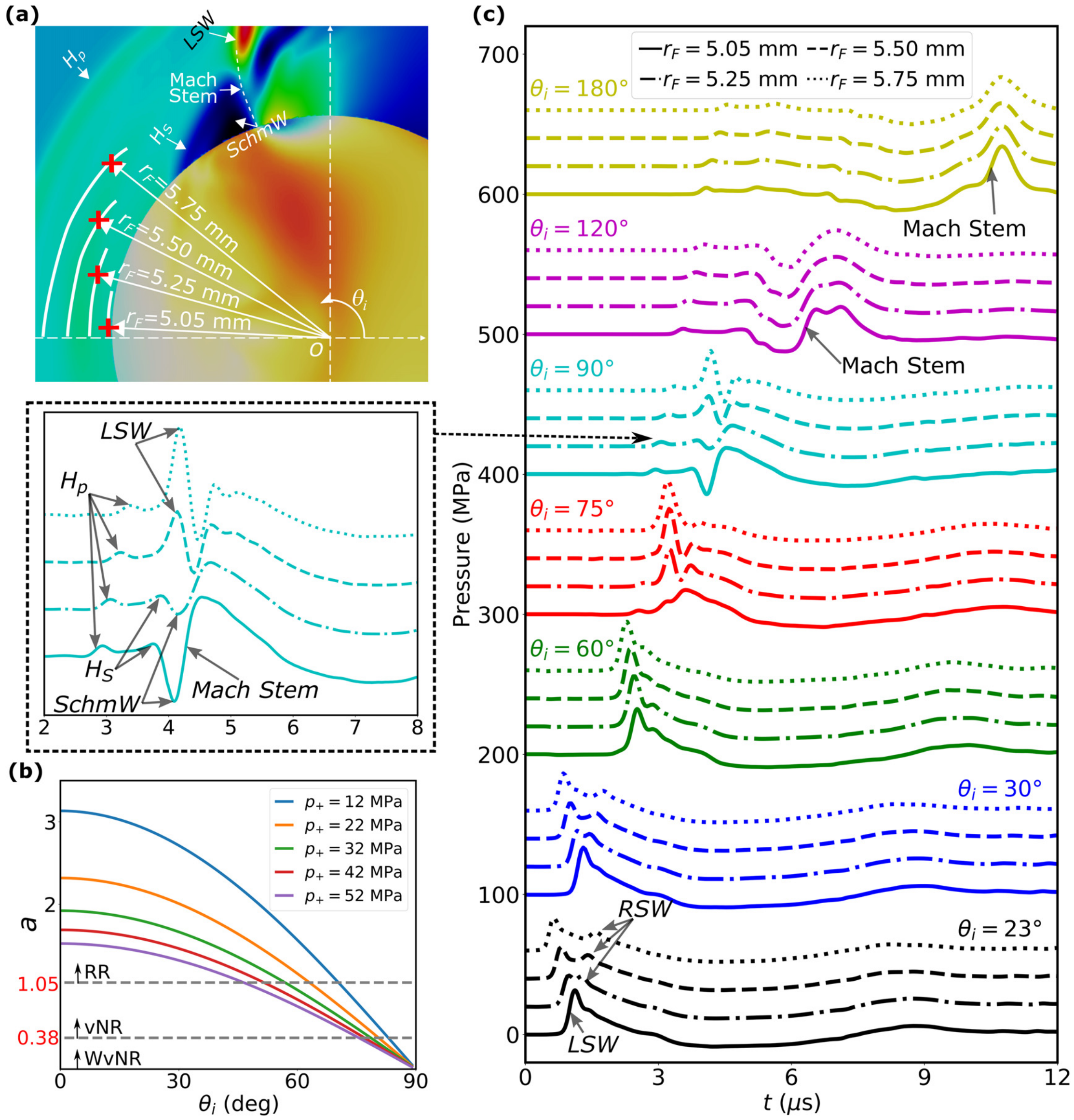

FIG. 8. (Color online) The variations of the pressure waveforms in the fluid near the stone boundary and associated critical parameter a for weak shock reflection at different incident angles (θ_i) or surface normal directions. (a) The schematic diagram for sensor placement at different radial distances (r_F) and θ_i. (b) The variation of the critical parameter a with θ_i in the range of p_+ for the incident LSW used in the experiment. The LSW-stone interaction will evolve from RR to vNR and WvNR as θ_i increases. (c) The time history of the pressure waveform variations in the fluid along different surface normal directions at $r_F = 5.05$, 5.25, 5.50, and 5.75 mm from the stone center under the condition of $r = -6$ mm. Note that the vertical scales are offset by 100 MPa for adjacent groups of θ_i and 20 MPa for adjacent values of r_F within a given θ_i.

$$a = \frac{\sin\varphi}{\sqrt{2\beta Ma}}, \tag{9}$$

where φ ($=90° - \theta_i$) is the grazing angle of the incident shock wave, β is the coefficient of nonlinearity of the propagation medium, which is equal to 5.1 for water at room temperature, and Ma ($=Ms - 1$) is the acoustic Mach number. The variation of the critical parameter a with θ_i in the range of p_+ for the incident LSW relevant to this study is plotted in Fig. 8(b). Based on previous studies (Karzova *et al.*, 2015), the weak shock reflection can be categorized into three regions (1) RR when $a > 1.05$, (2) von Neumann reflection (vNR) when $0.38 < a < 1.05$, and (3) weak von Neumann reflection (WvNR) when $a < 0.38$. It is generally observed that for a given p_+, the critical parameter a will decrease with θ_i in the range of 0°–90°, indicating that the LSW-stone interaction will evolve progressively from RR to vNR and then to WvNR. Furthermore, the critical θ_i for the transition from RR to vNR will decrease with p_+, varying from 71° at $p_+ = 12$ MPa to 46° at $p_+ = 52$ MPa. Similarly, the transition from vNR to WvNR will decrease from 83° at $p_+ = 12$ MPa to 75° at $p_+ = 52$ MPa. For the stone treated at $r = -6$ mm, it is anticipated that RR will be transitioned to vNR when θ_i is larger than 52° and then from vNR to WvNR when θ_i is larger than 75°.

Figure 8(c) depicts the pressure waveform variations along the stone boundary at various θ_i and r_F. At the beginning of the LSW-stone interaction ($\theta_i = 23°–30°$), RR dominates. Therefore, along each surface normal direction, as r_F increases, the first peak associated with the incident LSW will arrive earlier, and the second peak associated with the RSW will appear with an appreciable delay. At $\theta_i = 60^\circ$, when the weak shock reflection has transitioned into the vNR domain, the first peak starts to align closer with each other with increasing r_F, whereas the second peak becomes weaker or disappears, indicating the detachment of the point of intersection T from the stone boundary. At $\theta_i = 75^\circ$, the first peaks at different r_F (except $r_F = 5.05\,\text{mm}$) occur simultaneously, signifying the formation of a Mach stem along the surface normal direction. In contrast to the weak shock reflection from a rigid boundary, the fluid region in front of the Mach stem is significantly disturbed by the H_P, H_S, and Schmidt head wave emitted along the boundary ahead of the LSW. The influence of these leaky pressure waves first appears closest to the boundary (i.e., $r_F = 5.05\,\text{mm}$ at $\theta_i = 75^\circ$) before expanding outward (i.e., $r_F = 5.25 - 5.75\,\text{mm}$ at $\theta_i = 90^\circ$) during the transition from vNR to WvNR.

At the equator ($\theta_i = 90^\circ$), the H_P and H_S have clearly separated from the glancing incident LSW, which is further moving away from the stone boundary caused by the wave diffraction. Near the boundary ($r_F = 5.05$–$5.25\,\text{mm}$), a strong tensile peak is produced by the combination of the H_S and Schmidt head wave as shown in the inset of Fig. 8(c). Moreover, across the equator, the SAW produced by the LSW-stone interaction is transitioning from the LRW on the anterior to the Scholte wave on the posterior surface of the stone [see Figs. 7(d) and 7(e)]. Consequently, an inverted "*N*" wave is formed with a leading tensile component in the fin-shaped region produced by the H_S and Schmidt head wave in front of the Mach stem [see Fig. 8(a)], driven by the trailing compressive peak originated from the second hump (see Fig. 6 at 3.73 μs). As the Scholte wave propagates along the posterior surface, the leading tensile component of the pressure waveform broadens while the trailing compressive peak intensifies to generate higher pressure with a shortened pulse duration. Culminating at the north pole ($\theta_i = 180^\circ$), the Mach stem produces a high-pressure region normal to the stone boundary with a tail gradually tilting toward the upper half of the stone (see Fig. 6 at 10.8 μs).

We have further calculated the SI in the stone based on the Tuler-Butcher criterion for brittle failure under dynamical loading conditions (Tuler and Butcher, 1968; Zhang *et al.*, 2019):

$$\text{SI} = \int_0^{T_p} (\sigma_{\max} - \sigma_c)^2\, dt \quad \text{for } (\sigma_{\max} > \sigma_c), \tag{10}$$

where $\sigma_c = 3.1\,\text{MPa}$ is the quasi-static failure strength of soft BegoStone (Smith and Zhong, 2013), and $T_p = 12\,\mu\text{s}$ is the simulation time. As shown in Fig. 9(a), four sensors (M1–M4) are chosen from the T-shaped fracture region with sensors M1 located near the north pole, M2–M4 located about $D/3$ from the posterior surface of the stone, and the fifth sensor (M5) placed at the stone boundary along ray 3 where the peak $\sigma_{\max}$ is detected (see Fig. 7). As an illustrative example, Fig. 9(b) shows the time histories of $\sigma_{\max}$ at the five sensor locations in the stone treated at $r = -6\,\text{mm}$. In comparison, the highest tensile peak is produced at M5, followed by M1, M4, M3, and M2. It is noticed that despite similar time profiles in $\sigma_{\max}$, significantly higher tensile stresses are produced at M4 than at M2 because of the higher incident pressure of the LSW in the upper half of the stone. Furthermore, as shown in Fig. 9(c), significantly higher SI is predicted at M5 than at other sensor locations under asymmetric loading conditions (i.e., $r = -3$ to $-9\,\text{mm}$). This result suggests that when the stone is located off the lithotripter axis, there is a tendency that the crack may initiate from the stone boundary subjected to the high incident pressure of the LSW. In comparison, under the symmetric loading condition (i.e., $r = 0\,\text{mm}$), SI is slightly higher at M1 than at M5, whereas the comparable values are predicted at the other three sensor locations along the transverse crack inside the stone. This result is consistent with the T-shaped crack observed in the posterior region of the stone [Fig. 4(a)].

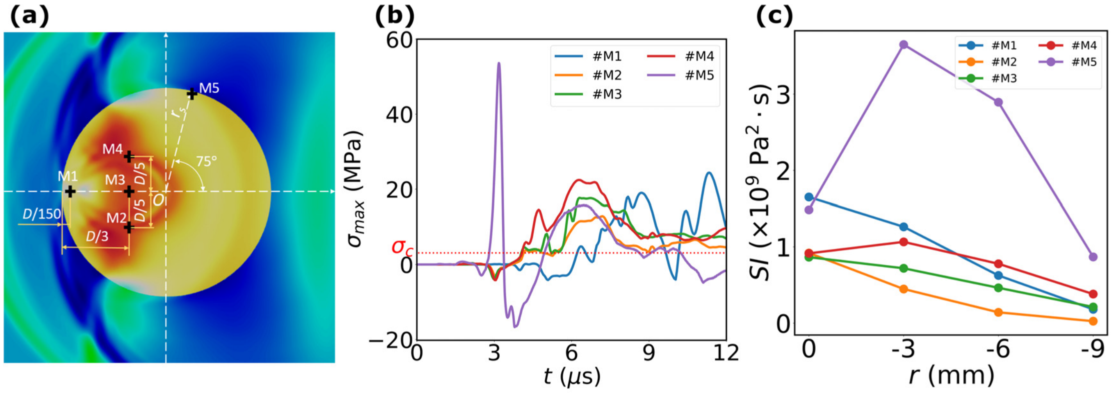

FIG. 9. (Color online) The variations of the stress field in the stone monitored by selected sensors imbedded near the periphery and in the posterior region of the stone. (a) The schematic diagram illustrating the sensor locations: M1 is chosen $D/150$ away from the north pole of the stone, M2–M4 are chosen $D/3$ away from the north pole, separated by $D/5$ spacing in the vertical direction, and M5 is chosen at the location where the peak in the maximum principal stress ($\sigma_{\max}$) occurs near the stone surface. (b) The time history of $\sigma_{\max}$ at individual sensor locations in the solid. (c) The SI based on the Tuler-Butcher criterion for the dynamic fracture for stones treated at four different off-axis radial distances in the lithotripter field.

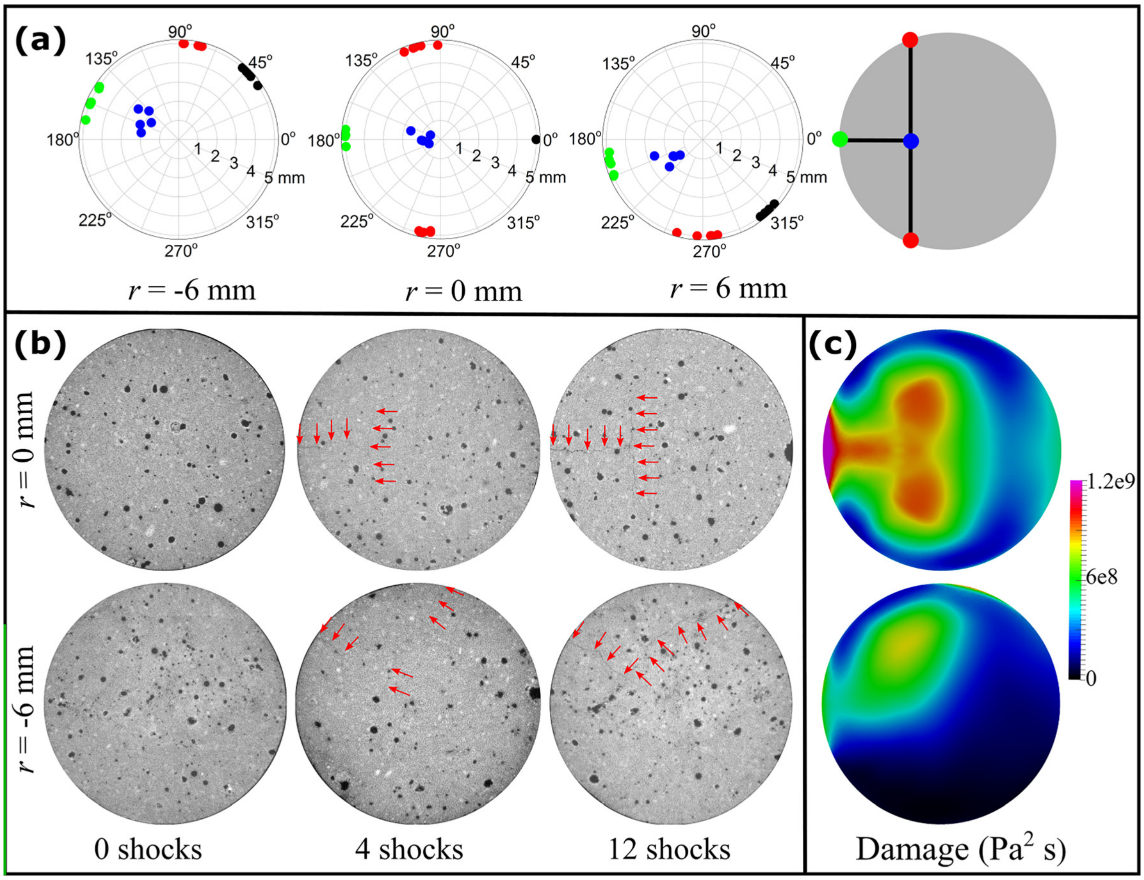

FIG. 10. (Color online) (a) The spatial distribution of the cavitation-generated damage crater location (black dot) on the anterior surface, junction point of the "*T*/*L*-shape" crack (blue dot), and interception points of crack lines on the lateral (red dot) and posterior (green dot) surface of the stone, (b) μCT images in the middle plane of the stone treated with a different number of shocks with red arrows indicating the hairline crack formation, and (c) damage potential computed based on the Tuler-Butcher criterion in the middle plane of the stone. Stone diameter = 10 mm.

C. Examinations of crack initiation and development using μCT

To confirm the general features of the stone fracture at various lithotripter field positions observed from experiments in Sec. III A 2 and predicted by numerical simulations in Sec. III B, we further investigated the crack initiation and development under symmetric ($r = 0$ mm) and asymmetric ($r = -6$ mm) loading conditions using μCT. Figure 10(a) is a scatterplot summarizing the spatial distribution of the cavitation-generated damage crater location (black dot) on the anterior surface, the junction point of the "*T*- or *L*-shape" crack (blue dot), and the interception points of the crack lines on the lateral (red dot) and posterior (green dot) surface of the stone samples. To capture the crack initiation, additional experiments were repeated using only 4 or 12 shocks before visible crack lines could be observed (typically after about 17 shocks at $r = 0$ mm and 19 shocks at $r = -6$ mm; see Table III). Representative μCT images, captured either before or after the treatment, from the middle plane of the samples are shown in Fig. 10(b). It can be seen that under symmetric loading conditions ($r = 0$ mm), a longitudinal hairline crack was initiated from the north pole and a transverse hairline crack centered around the lithotripter axis at a distance about *D*/3 from the posterior surface of the stone appeared after four shocks. After treatment of 12 shocks, the longitudinal crack was fully extended to the junction point with the transverse crack, which was further opened and extended both upward and downward to the stone surface. In contrast, under asymmetric loading conditions ($r = -6$ mm), two short hairline cracks were initiated from the upper stone boundary—one at about 80° and the other at about 150° after four shocks—in the range of the interception points shown in Fig. 10(a). After 12 shocks, these 2 short cracks were seen to extend into the bulk of the stone, forming the *L*-shaped crack. Overall, these crack initiation positions are consistent with the locations of the highest SI predicted in the stone, based on the numerical model simulations shown in Figs. 10(c) and 9(c).

IV. DISCUSSION AND SUMMARY

To understand the mechanism of stone damage in SWL under clinically relevant treatment conditions, we have performed a comprehensive series of investigations using high-speed photoelastic imaging, phantom tests, μCT analysis, and 3D numerical simulation of the transient stress field and fracture potential produced in BegoStone samples located at various lateral positions in a lithotripter field. Recently, photoelastic imaging has also been applied effectively to burst wave lithotripsy studies (Maxwell *et al.*, 2020; Sapozhnikov *et al.*, 2020). In the present work, several critical and novel observations have been made.

First, because of the significant respiratory motion of the patient during clinical SWL (Bohris *et al.*, 2003; Pishchalnikov *et al.*, 2006; Leighton *et al.*, 2008; Sorensen *et al.*, 2012), most of the LSW-stone interaction will likely occur at off-axis locations. Under such conditions, our results (Figs. 6, 7, and 9) suggest that the maximum tensile stress and SI will be produced on the stone boundary subjected to the higher incident pressure of the LSW. This finding is consistent with the previous experimental observations that stone comminution in SWL correlates closely with the average positive peak pressure ($p_{+(\mathrm{avg})}$) of the incident LSW on the stone surface in the lithotripter field (Smith and Zhong, 2012; Zhang *et al.*, 2016). This finding is also in distinct contrast to the generation of the maximum tensile stress and/or SI inside the stone produced in the posterior region by wave focusing and constructive interactions when the stone is ideally treated on the lithotripter axis (see Fig. 5 and also Cleveland and Sapozhnikov, 2005; Zhang *et al.*, 2016; Cao *et al.*, 2019). With irregular geometry of the residual fragments and attenuation of various elastic waves inside the stone material, which are not yet accounted for in the model simulations, the possibility of stone fracture from inside-out will further diminish, whereas the chance of stone fracture from outside-in is likely to increase during SWL (Zhong, 2013; Neisius and Zhong, 2019).

Second, tensile and shear stresses are efficiently produced by mode conversion on the stone boundary during LSW-stone interaction (Xi and Zhong, 2001; Cleveland and Sapozhnikov, 2005; Sapozhnikov *et al.*, 2007; Zhong, 2013). The current study further elucidates the critical role that LRW and its dynamic interaction with an EW simultaneously produced on the fluid side in the buildup of the maximum tensile stress along the stone boundary (Fig. 7 and see also Zhang *et al.*, 2019). The mode conversion of the incident LSW into LRW confined to the stone surface is much more efficient than the generation of P and S waves that spread into the bulk of the stone material, leading to maximum SI that drives the initiation of fractures on the anterior surface of the stone treated at off-axis locations (Fig. 10). In contrast, the strong tensile stress produced in the posterior region of the stone is caused primarily by the reflection of the S wave (i.e., S-P and S-S) and P wave (i.e., P-P and P-S) and their interactions (Figs. 5 and 6).

Third, we have shown shock front detachment from the stone boundary and Mach stem formation based on the sensor data analysis. Our results indicate a clear transition from RR to vNR and then to WvNR with increasing θ_i, which is in reasonable agreement with the prediction based on the critical parameter "a" for the weak shock reflection (Baskar *et al.*, 2007; Karzova *et al.*, 2015). The formation of the Mach stem is initiated when the shock wave reflection pattern is transitioning from RR to vNR. Thereafter, the Mach stem grows progressively in strength and length as the LSW-stone interaction induced SAWs transitioning from the LRW on the anterior surface to the Scholte wave on the posterior surface of the stone (Figs. 6 and 8). Unlike the shock reflection from a rigid boundary (Zakharian *et al.*, 2000; Skews and Ashworth, 2005; Baskar *et al.*, 2007), we notice that the Mach stem formation in SWL is significantly influenced by the H_P, H_S, and Schmidt head wave emitted along the stone boundary ahead of the LSW.

Finally, cavitation erosion is observed on the anterior surface of the stone either along or near the central axis of the incident LSW, separated from the fracture lines (Fig. 4). The interaction of LSWs or SAWs produced by the incident LSW with the pitting and microfractures generated by cavitation damage may further facilitate the disintegration of residual fragments in SWL (Zhu *et al.*, 2002; Sapozhnikov *et al.*, 2007; Zhong, 2013). Yet, the mechanism of such an interaction is not completely clear and needs to be further investigated.

In summary, we have investigated the generation of SAWs and Mach stem in SWL and provide new insights into the mechanisms of stone fracture under asymmetric loading conditions during LSW-stone interaction. Future work is warranted to examine the optimal treatment strategy that can leverage the synergistic interaction of multiple mechanisms to maximize stone comminution in SWL.

ACKNOWLEDGMENTS

This work is supported by the National Institutes of Health (NIH) through Grant Nos. 5R37DK052985-23 and 2R01DK052985-24A1. S.C. and K.W. gratefully acknowledge the support of the National Science Foundation (NSF) under Award Nos. CBET-1751487 and CBET-1706003, respectively.

Alelign, T., and Petros, B. (**2018**). "Kidney stone disease: An update on current concepts," Adv. Urol. **2018**, 3068365.

Assimos, D., Krambeck, A., Miller, N. L., Monga, M., Murad, M. H., Nelson, C. P., Pace, K. T., Pais, V. M., Jr., Pearle, M. S., Preminger, G. M., Razvi, H., Shah, O., and Matlaga, B. R. (**2016**). "Surgical management of stones: American Urological Association/Endourological Society Guideline, Part II," J. Urol. **196**, 1161–1169.

Averkiou, M. A., and Cleveland, R. O. (**1999**). "Modeling of an electrohydraulic lithotripter with the KZK equation," J. Acoust. Soc. Am. **106**, 102–112.

Baskar, S., Coulouvrat, F., and Marchiano, R. (**2007**). "Nonlinear reflection of grazing acoustic shock waves: Unsteady transition from von Neumann to Mach to Snell-Descartes reflections," J. Fluid. Mech. **575**, 27–55.

Bohris, C., Bayer, T., and Lechner, C. (**2003**). "Hit/miss monitoring of ESWL by spectral Doppler ultrasound," Ultrasound Med. Biol. **29**, 705–712.

Cao, S., Zhang, Y., Liao, D., Zhong, P., and Wang, K. G. (**2019**). "Shock-induced damage and dynamic fracture in cylindrical bodies submerged in liquid," Int. J. Solids Struct. **169**, 55–71.

Carcione, J. M., Bagaini, C., Ba, J., Wang, E. J., and Vesnaver, A. (**2018**). "Waves at fluid–solid interfaces: Explicit versus implicit formulation of the boundary condition," Geophys. J. Int. **215**, 37–48.

Chaussy, C., Schuller, J., Schmiedt, E., Brandl, H., Jocham, D., and Liedl, B. (**1984**). "Extracorporeal shock-wave lithotripsy (ESWL) for treatment of urolithiasis," Urology **23**, 59–66.

Cleveland, R. O., Anglade, R., and Babayan, R. K. (**2004**). "Effect of stone motion on *in vitro* comminution efficiency of Storz Modulith SLX," J. Endourol. **18**, 629–633.

Cleveland, R. O., and Sapozhnikov, O. A. (**2005**). "Modeling elastic wave propagation in kidney stones with application to shock wave lithotripsy," J. Acoust. Soc. Am. **118**, 2667–2676.

Eisenmenger, W. (**2001**). "The mechanisms of stone fragmentation in ESWL," Ultrasound Med. Biol. **27**, 683–693.

Esch, E., Simmons, W. N., Sankin, G., Cocks, H. F., Preminger, G. M., and Zhong, P. (**2010**). "A simple method for fabricating artificial kidney stones of different physical properties," Urol. Res. **38**, 315–319.

Farhat, C., Gerbeau, J.-F., and Rallu, A. (**2012**). "FIVER: A finite volume method based on exact two-phase Riemann problems and sparse grids for multi-material flows with large density jumps," J. Comput. Phys. **231**, 6360–6379.

Farhat, C., Rallu, A., Wang, K., and Belytschko, T. (**2010**). "Robust and provably second-order explicit-explicit and implicit-explicit staggered time-integrators for highly non-linear compressible fluid-structure interaction problems," Int. J. Numer. Meth. Eng. **84**, 73–107.

Fovargue, D., Mitran, S., Sankin, G., Zhang, Y., and Zhong, P. (**2018**). "An experimentally-calibrated damage mechanics model for stone fracture in shock wave lithotripsy," Int. J. Fracture **211**, 203–216.

Fovargue, D. E., Mitran, S., Smith, N. B., Sankin, G. N., Simmons, W. N., and Zhong, P. (**2013**). "Experimentally validated multiphysics computational model of focusing and shock wave formation in an electromagnetic lithotripter," J. Acoust. Soc. Am. **134**, 1598–1609.

Freund, L. B. (**1998**). *Dynamic Fracture Mechanics* (Cambridge University Press, Cambridge, UK).

Gracewski, S. M., Dahake, G., Ding, Z., Burns, S. J., and Everbach, E. C. (**1993**). "Internal stress wave measurements in solids subjected to lithotripter pulses," J. Acoust. Soc. Am. **94**, 652–661.

Johnsen, E., and Colonius, T. (**2006**). "Implementation of WENO schemes in compressible multicomponent flow problems," J. Comput. Phys. **219**, 715–732.

Karzova, M. M., Khokhlova, V. A., Salze, E., Ollivier, S., and Blanc-Benon, P. (**2015**). "Mach stem formation in reflection and focusing of weak shock acoustic pulses," J. Acoust. Soc. Am. **137**, EL436–EL442.

Kronenberg, P., and Somani, B. (**2018**). "Advances in lasers for the treatment of stones—A systematic review," Curr. Urol. Rep. **19**, 45.

Leighton, T., Fedele, F., Coleman, A., McCarthy, C., Ryves, S., Hurrell, A., De Stefano, A., and White, P. (**2008**). "A passive acoustic device for real-time monitoring of the efficacy of shockwave lithotripsy treatment," Ultrasound Med. Biol. **34**, 1651–1665.

Lingeman, J. E., McAteer, J. A., Gnessin, E., and Evan, A. P. (**2009**). "Shock wave lithotripsy: Advances in technology and technique," Nat. Rev. Urol. **6**, 660–670.

Lokhandwalla, M., and Sturtevant, B. (**2000**). "Fracture mechanics model of stone comminution in ESWL and implications for tissue damage," Phys. Med. Biol. **45**, 1923–1940.

Main, A., Zeng, X., Avery, P., and Farhat, C. (**2017**). "An enhanced FIVER method for multi-material flow problems with second-order convergence rate," J. Comput. Phys. **329**, 141–172.

Marchiano, R., Coulouvrat, F., Baskar, S., and Thomas, J. L. (**2007**). "Experimental evidence of deviation from mirror reflection for acoustical shock waves," Phys. Rev. E **76**, 056602.

Matlaga, B. R., Chew, B., Eisner, B., Humphreys, M., Knudsen, B., Krambeck, A., Lange, D., Lipkin, M., Miller, N. L., Monga, M., Pais, V., Sur, R. L., and Shah, O. (**2018**). "Ureteroscopic laser lithotripsy: A review of dusting vs fragmentation with extraction," J. Endourol. **32**, 1–6.

Maxwell, A. D., MacConaghy, B., Bailey, M. R., and Sapozhnikov, O. A. (**2020**). "An investigation of elastic waves producing stone fracture in burst wave lithotripsy," J. Acoust. Soc. Am. **147**, 1607–1622.

Neisius, A., Smith, N. B., Sankin, G., Kuntz, N. J., Madden, J. F., Fovargue, D. E., Mitran, S., Lipkin, M. E., Simmons, W. N., and Preminger, G. M. (**2014**). "Improving the lens design and performance of a contemporary electromagnetic shock wave lithotripter," Proc. Natl. Acad. Sci. U.S.A. **111**, E1167–E1175.

Neisius, A., and Zhong, P. (**2019**). "Physics of shock-wave lithotripsy," in *Smith's Textbook of Endourology*, edited by A. D. Smith, G. M. Preminger, L. R. Kavoussi and G. H. Badlani (Quality Medical Publishing, St. Louis), pp. 689–712.

New, F., and Somani, B. K. (**2016**). "A complete world literature review of quality of life (QOL) in patients with kidney stone disease (KSD)," Curr. Urol. Rep. **17**, 88.

Pawar, A. S., Thongprayoon, C., Cheungpasitporn, W., Sakhuja, A., Mao, M. A., and Erickson, S. B. (**2018**). "Incidence and characteristics of kidney stones in patients with horseshoe kidney: A systematic review and meta-analysis," Urol. Ann. **10**, 87–93.

Pishchalnikov, Y. A., Neucks, J. S., VonDerHaar, R. J., Pishchalnikova, I. V., Williams, J. C., and McAteer, J. A. (**2006**). "Air pockets trapped during routine coupling in dry head lithotripsy can significantly decrease the delivery of shock wave energy," J. Urol. **176**, 2706–2710.

Qin, J., Simmons, W. N., Sankin, G., and Zhong, P. (**2010**). "Effect of lithotripter focal width on stone comminution in shock wave lithotripsy," J. Acoust. Soc. Am. **127**, 2635–2645.

Sapozhnikov, O. A., Maxwell, A. D., and Bailey, M. R. (**2020**). "Modeling of photoelastic imaging of mechanical stresses in transparent solids mimicking kidney stones," J. Acoust. Soc. Am. **147**, 3819–3829.

Sapozhnikov, O. A., Maxwell, A. D., MacConaghy, B., and Bailey, M. R. (**2007**). "A mechanistic analysis of stone fracture in lithotripsy," J. Acoust. Soc. Am. **121**, 1190–1202.

Schröder, C. T., and Scott, W. R., Jr. (**2001**). "On the complex conjugate roots of the Rayleigh equation: The leaky surface wave," J. Acoust. Soc. Am. **110**, 2867–2877.

Skews, B. W., and Ashworth, J. T. (**2005**). "The physical nature of weak shock wave reflection," J. Fluid. Mech. **542**, 105–114.

Smith, N., and Zhong, P. (**2012**). "Stone comminution correlates with the average peak pressure incident on a stone during shock wave lithotripsy," J. Biomech. **45**, 2520–2525.

Smith, N. B., and Zhong, P. (**2013**). "A heuristic model of stone comminution in shock wave lithotripsy," J. Acoust. Soc. Am. **134**, 1548–1558.

Sorensen, M. D., Bailey, M. R., Shah, A. R., Hsi, R. S., Paun, M., and Harper, J. D. (**2012**). "Quantitative assessment of shockwave lithotripsy accuracy and the effect of respiratory motion," J. Endourol. **26**, 1070–1074.

Sturtevant, B. (**1996**). "Shock wave physics of lithotriptors," in *Smith's Textbook of Endourology*, edited by A. D. Smith, G. H. Badlani, and D. H. Bagley (Quality Medical Publishing, St. Louis), pp. 529–552.

Tuler, F. R., and Butcher, B. M. (**1968**). "A criterion for the time dependence of dynamic fracture," Int. J. Fract. Mech. **4**, 431–437.

Turk, C., Petrik, A., Sarica, K., Seitz, C., Skolarikos, A., Straub, M., and Knoll, T. (**2016**). "EAU guidelines on interventional treatment for urolithiasis," Eur. Urol. **69**, 475–482.

Viktorov, I. A. (**1967**). *Rayleigh and Lamb Waves: Physical Theory and Applications* (Plenum, New York).

Wang, K., Grétarsson, J., Main, A., and Farhat, C. (**2012**). "Computational algorithms for tracking dynamic fluid–structure interfaces in embedded boundary methods," Int. J. Numer. Meth. Fluids **70**, 515–535.

Wang, K., Rallu, A., Gerbeau, J. F., and Farhat, C. (**2011**). "Algorithms for interface treatment and load computation in embedded boundary methods for fluid and fluid-structure interaction problems," Int. J. Numer. Meth. Fluids **67**, 1175–1206.

Wang, K. G. (**2017**). "Multiphase fluid-solid coupled analysis of shock-bubble-stone interaction in shockwave lithotripsy," Int. J. Numer. Method Biomed. Eng. **33**, e2855.

Wijerathne, M., Hori, M., Sakaguchi, H., and Oguni, K. (**2010**). "3D dynamic simulation of crack propagation in extracorporeal shock wave lithotripsy," in *IOP Conference Series: Materials Science and Engineering* (IOP Publishing), p. 012120.

Xi, X., and Zhong, P. (**2001**). "Dynamic photoelastic study of the transient stress field in solids during shock wave lithotripsy," J. Acoust. Soc. Am. **109**, 1226–1239.

Zakharian, A. R., Brio, M., Hunter, J. K., and Webb, G. M. (**2000**). "The von Neumann paradox in weak shock reflection," J. Fluid. Mech. **422**, 193–205.

Zhang, Y., Nault, I., Mitran, S., Iversen, E. S., and Zhong, P. (**2016**). "Effects ofs size on the comminution process and efficiency in shock wave lithotripsy," Ultrasound. Med. Biol. **42**, 2662–2675.

Zhang, Y., Yang, C., Qiang, H., and Zhong, P. (**2019**). "Nanosecond shock wave-induced surface acoustic waves and dynamic fracture at fluid-solid boundaries," Phys. Rev. Res. **1**, 033068.

Zhong, P. (**2013**). "Shock wave lithotripsy," in *Bubble Dynamics and Shock Waves*, edited by C. F. Delale (Springer, Berlin), pp. 291–338.

Zhong, P., Chuong, C., and Preminger, G. (**1993**). "Characterization of fracture toughness of renal calculi using a microindentation technique," J. Mater. Sci. Lett. **12**, 1460–1462.

Zhu, J. Y., Popovics, J. S., and Schubert, F. (**2004**). "Leaky Rayleigh and Scholte waves at the fluid–solid interface subjected to transient point loading," J. Acoust. Soc. Am. **116**, 2101–2110.

Zhu, S., Cocks, F. H., Preminger, G. M., and Zhong, P. (**2002**). "The role of stress waves and cavitation in stone comminution in shock wave lithotripsy," Ultrasound. Med. Biol. **28**, 661–671.